Thermal history of Northwest Africa 5073–A coarse-grained Stannern-trend eucrite containing cm-sized pyroxenes and large zircon grains

Julia Roszjar, Knut Metzler, Addi Bischoff, Jean-Alix J-A Barrat, Thorsten Geisler, R.C. Greenwood, I. A. Franchi, Stephan Klemme

Thermal history of Northwest Africa (NWA) 5073 - a coarse-grained Stannern-trend eucrite containing cm-sized pyroxenes and large zircon grains

Julia Roszjar[1], Knut Metzler[1], Addi Bischoff[1], Jean-Alix Barrat[2], Thorsten Geisler[3], Richard C. Greenwood[4], Ian A. Franchi[4], and Stephan Klemme[5]

[1]Institut für Planetologie, Westfälische Wilhelms-Universität Münster, Wilhelm-Klemm-Str. 10, D-48149 Münster, Germany (e-mail: j_rosz01@uni-muenster.de).

[2]Université Européenne de Bretagne, Institut Universitaire Européen de la Mer, Place Nicolas Copernic, 29280 Plouzané Dedex, France.

[3]Steinmann Institut, Rheinische Friedrich-Wilhelms-Universität Bonn, Poppelsdorfer Schloß, 53115 Bonn, Germany

[4]Planetary and Space Sciences Research Institute, The Open University, Milton Keynes, MK7 6AA, UK.

[5]Institut für Mineralogie, Westfälische Wilhelms-Universität Münster, Corrensstr. 24, D-48149 Münster, Germany.

Abstract

We report on the bulk chemical composition, petrology, oxygen isotopic composition, trace element composition of silicates, and degree of self-irradiation damage on zircon grains of the eucrite Northwest Africa (NWA) 5073, to constrain its formation and post-crystallization thermal history, and to discuss their implications for the geologic history of its parent body. This unequilibrated and unbrecciated meteorite is a new member of the rare Stannern-trend eucrites. It is mainly composed of elongated, zoned pyroxene phenocrysts up to 1.2 cm, plagioclase laths up to 0.3 cm in length, and is rich in mesostasis. The latter contains zircon grains up to 30 μm in diameter, metal, sulfide, tridymite, and Ca-phosphates. Textural observations and silicate compositions coupled with the occurrence of extraordinary Fe-rich olivine veins that are restricted to large pyroxene laths indicate that NWA 5073 underwent a complex thermal history. This is also supported by the annealed state of zircon grains inferred from μ-Raman spectroscopic measurements along with U and Th data obtained by electron probe microanalyses.

Keywords: eucrite, bulk chemistry, petrology, trace elements, oxygen isotopes, μ-Raman spectroscopy, zircon annealing

Introduction

The so-called HED suite of achondrites (Howardites, Eucrites, and Diogenites) makes up the largest suite of igneous rocks available from any Solar System body besides the Earth and the Moon (Mittlefehldt et al., 1998). Eucrites represent basaltic rocks and gabbroic cumulates, whereas diogenites are ultramafic rocks (orthopyroxenites, olivine-bearing orthopyroxenites, harzburgites, and dunites), mainly composed of orthopyroxene and olivine (e.g., Mittlefehldt et al., 1998; Beck and McSween, 2010). Howardites are polymict breccias, consisting of various amounts of eucritic and diogenitic lithologies. The close relationship between HEDs is convincingly supported by petrographic, mineralogical, chemical, and isotopic evidences (see McSween et al., 2010 for a review), and suggest that they derived from the same parent body, possibly the asteroid 4 Vesta (e.g., McCord et al., 1970; Consolmagno and Drake, 1977; Binzel and Xu, 1993; Drake, 2001). However, a few eucrites display unusual petrographic features and distinct oxygen isotopic compositions and could, therefore, have originated from distinct parent bodies (e.g., Yamaguchi et al., 2002; Scott et al., 2009; Gounelle et al., 2009; Bland et al., 2009). Eucrites are widely thought to represent either surface or near-surface basaltic liquids (lava flows or shallow intrusions) or crystal accumulations from basaltic liquids. Most eucrites experienced a complex post-crystallization history, including prolonged thermal metamorphism that produced recrystallization textures and caused exsolution and inversion of pyroxenes (e.g., Takeda and Graham, 1991; Metzler et al., 1995, Yamaguchi et al., 1996, 2009; Mayne et al., 2009), and multiple impact events. Thus, many eucrites are brecciated, and were formed in the regolith and mega-regolith of their parent body (e.g., Stöffler et al., 1988). They consist of mineral and/or lithic fragments embedded in a fine-grained, generally fragmented matrix (e.g., Takeda and Graham, 1991; Metzler et al., 1995; Bischoff et al., 2006; Llorca et al., 2009). From a chemical point of view, eucrites can be subdivided into basaltic (noncumulate), and cumulate eucrites, both of which occur also as clasts in polymict eucrites and howardites (e.g., Takeda, 1991). Cumulate eucrites are coarse-grained rocks with high Mg-numbers [Mg# = molar Mg/(Mg + Fe)], low incompatible trace element abundances compared to other eucrites, and pronounced positive Eu anomalies - a feature consistent with plagioclase accumulation. Basaltic eucrites can be subdivided into three compositional distinct groups on the basis of their Mg# or FeO_{total}/MgO wt.% ratio, TiO_2 contents, and incompatible trace element abundances (e.g., Stolper, 1977; Warren and Jerde, 1987; Mittlefehldt et al., 1998; Yamaguchi et al., 2009): Main Group Nuevo Laredo-trend eucrites, Stannern-trend eucrites and the residual eucrites. Main Group Nuevo Laredo-trend eucrites are the most common ones. They display wide variations in Mg# with only moderate variations in incompatible element abundances. They are believed to represent a fractional crystallization trend (e.g., Stolper, 1977; Warren and Jerde, 1987). Stannern-trend eucrites are rare. They include three falls (Stannern, Bouvante, and Pomozdino), and about a dozen finds from Antarctica (e.g., Y-75011) and from the Sahara (e.g., NWA 4523 and NWA 1000). They display the same major element abundances as the less evolved rocks of the Nuevo Laredo group, but exhibit high Ti and incompatible trace element abundances, and significant negative

Eu, Sr, and Be anomalies. The origin of these eucrites is controversial. It has been proposed that the Stannern-trend eucrites could have been generated from the same mantle source as Main Group eucrites but at smaller degrees of partial melting, and possibly at slightly different oxygen fugacities (Stolper, 1977; Mittlefehldt and Lindstrom, 2003). Alternatively, it has been proposed that the high incompatible trace element abundances could be explained by an intricate in-situ crystallization process (Barrat et al., 2000), or by the involvement of highly evolved KREEP-like melts (Warren and Kallemeyn, 2001). The contamination of Main Group eucritic magmas might be also explained by melts derived from partial melting of the asteroid's crust, which would can successfully explain both the high incompatible trace elements concentrations and the distinctive Eu, Sr, and Be anomalies shown by the Stannern-trend eucrites (Barrat et al., 2007). Finally, the residual eucrites display major element abundances consistent with Main Group eucrites, but light REE depletions and positive Eu anomalies. Partial melting followed by extraction of a few percent of partial melts can satisfactorily explain these features (Yamaguchi et al., 2009). At present, it is generally thought that the differentiation history of the eucrite parent body has been triggered by the formation of a global magma ocean (e.g., Takeda, 1979; Righter and Drake, 1997; Ruzicka et al., 1997; Warren, 1997; Greenwood et al., 2005). This hypothesis is at first glance consistent with the petrology of the eucrites, but cannot easily account for the geochemistry of the diogenites (e.g., Mittlefehldt 2000; Barrat et al., 2008, 2010). Thus, the magmatic and thermal histories of the parent body were certainly much more complicated than generally believed and more detailed studies of HED meteorites are necessary to further our understanding of the process leading to the formation of HED meteorite genesis. Recently, we have identified NWA 5073, a eucrite which displays some unique features. This single, unbrecciated stone is characterized by an unusual texture with cm-sized unequilibrated pyroxenes crosscut by numerous secondary olivine-rich veins, and mesostasis areas containing large zircon grains. Here, we report on the bulk chemistry, petrology, and isotopic characteristics of this exceptional meteorite and discuss its genesis and complex post-crystallization history. Preliminary data on NWA 5073 have been previously presented by Roszjar et al. (2009a-c) and Roszjar and Scherer (2010).

Analytical Methods

The textural and mineralogical investigations of the sample were performed by optical and electron microscopy on a thin section (PL07217). Modal abundance of major phases and mesostasis were determined based on multiple point-counting applied on a backscattered electron (BSE) photomicrograph using an Olympus Analysis software. A JEOL A840 scanning electron microscope (SEM) equipped with energy dispersive spectrometers (EDS; INCA; Oxford Instrument) at the Interdisciplinary Center for Electron Microscopy and Microanalysis (ICEM) at the Westfälische Wilhelms-Universität Münster was used for detailed petrographic investigations. Qualitative analyses have been carried out using an acceleration voltage of 20 kV, and a beam current of 15 nA. High

contrast, low brightness BSE imaging has been used for systematic identification and localization of Zr-bearing phases. Quantitative analyses of mineral compositions were obtained using a JEOL JXA 8900 Superprobe electron probe micro analyzer (EPMA) operated at an acceleration voltage and beam current of 15 kV and 15 nA, respectively. Natural and synthetic standards of well-known compositions were used as standards. Matrix corrections were made according to the $\Phi\rho(z)$ procedure of Armstrong (1991).

Prior to micro-Raman spectroscopy, investigations of zircon grains were performed on the JEOL A840 SEM at conditions described above. BSE imaging allowed selection of 10 appropriate grains with sufficient diameter ranging from 10-25 μm that were free of cracks and inclusions, and were representative of the whole zircon population in NWA 5073 in terms of mineral shape and mineral paragenesis with surrounding phases. The same spots on individual zircon grains investigated by Raman spectroscopy were subsequently analyzed for major, minor, and trace element concentrations by wavelength-dispersive analysis using a Cameca SX 100 EPMA at the Institut für Mineralogie, Universität Hamburg. Major (Si, Zr, Hf) and minor (Al, Fe, P, Ca, Mn, Y) elements were analyzed in a first sequence using a beam current of 20 nA, an acceleration voltage of 15 keV, total counting times of 30 s, and a beam diameter of 1-2 μm. Th and U concentrations were subsequently determined in a separate cycle with total counting times of 600 s (10 × 60 s) for the U-M_β and Th-M_α line, and a beam current and acceleration voltage of 200 nA and 15 kV, respectively, to achieve a better precision. A small overlap of the Th-M_α on the U-M_β line was corrected using the method proposed by Åmli & Griffin (1975). For these conditions the detection limit of U and Th is about 20-30 ppm.

Micro-Raman spectroscopic measurements were performed subsequently, but prior to compositional analysis by EPMA to preclude any possible irreversible modifications of the radiation-damaged structure as a result of the electron beam impact. Micro-Raman spectroscopic analyses were carried out on a polished, cleaned thin section of NWA 5073 using a Jobin Yvon HR800 dispersive Raman spectrometer at the Institut für Anorganische und Analytische Chemie at the Westfälische Wilhelms-Universität Münster. The 632.187 nm line of a Nd-YAG laser was used as excitation source with a beam power of ~10 mW at the exit of the laser. The scattered Raman light was collected with a 100 times objective (N.A. =0.9) with charge-coupled device detector (CCD) after being dispersed by a grating of 1800 grooves mm^{-1}. The spectrometer slit width was set to 150 μm, yielding a spectral resolution of 1.9 cm^{-1} near 1000 cm^{-1} as determined from Ne light bands. The lateral resolution was about 1-2 μm. A possible spectrometer drift was monitored by measuring the 520.7 cm^{-1} band of silicon and the spectral lines of the Ne-lamp immediately before and after the sample analyses. Information about the structural state of individual zircon grains was obtained by examining the total spectrum and by monitoring the intensity, full width at half maximum (FWHM), and the frequency of the internal antisymmetric $\nu_3(SiO_4)$ stretching mode located near 1008 cm^{-1} in a non-metamict zircon. This band was monitored because (i) it has been shown that it is most suitable for quantifying

radiation damage (Wopenka et al., 1996; Nasdala et al., 1996; Nasdala et al., 1998; Palenik et al., 2003), since it is the strongest Raman band of zircon and thus easy to measure precisely (Dawson et al., 1971; Nasdala et al., 1996; Zhang et al., 2000a), and (ii) it is not significantly red-shifted by impurity-related structural disorder such as caused by variations in the Hf concentration (Hoskin and Rodgers, 1996). The broad band profile in the frequency region between 900 and 1100 cm^{-1} results from an overlap of the $\nu_3(SiO_4)$ with the adjacent, internal $\nu_1(SiO_4)$ stretching mode (A_{1g} symmetry; Dawson et al., 1971) at about 975 cm^{-1} and, in radiation-damaged zircon, from the contribution of a broad background feature at a lower frequency, which has been assigned to the amorphous component in metamict zircon (Zhang et al., 2000a). Quantitative band parameters were obtained by deconvoluting the overall band profile in the frequency region between 800 and 1100 cm^{-1} with three Voigt functions and a linear background as shown by Geisler et al. (2001). The reproducibility of the fitted frequency is better than 0.2 cm^{-1} and that of the linewidth is in the order of ±0.5 cm^{-1} at a linewidth smaller than 20 cm^{-1} and ±1.0 cm^{-1} for larger linewidths. The effect of the finite slit width on the measured linewidth, given as the full width at half maximum (FWHM), was then corrected by the method of Tanabe and Hiraishi (1980).

From radioactive decay of the ^{238}U, ^{235}U, and ^{232}Th isotopes, the number of α-decay events for different U and Th concentrations were calculated according to the following equation:

$$D_\alpha = 8\,N_1\,[exp(\lambda_1 t - 1)] + 7\,N_2\,[exp(\lambda_2 t - 1)] + 6\,N_3\,[exp(\lambda_3 t - 1)] \quad (1)$$

where N_1, N_2, and N_3 are the present concentrations of ^{238}U, ^{235}U, and ^{232}Th in the zircon grains, respectively, λ_1, λ_2, and λ_3 are the decay constants for ^{238}U, ^{235}U, and ^{232}Th in years $^{-1}$, respectively, and t is the age of the zircon. For our calculations we assumed an age of 4.55 Ga.

The bulk chemical composition of NWA 5073 has been determined at the Institut Universitaire Européen de la Mer (IUEM), Plouzané, using ~100 mg of powdered sample material. The powdered whole rock fraction, derived from initially ~12 g sample material and devoid of fusion crust, was precleaned with ethanol and ultra pure MilliQ® water in an ultrasonic bath, before it was carefully crushed into small pieces in an agate mortar. Subsequently, a representative fraction of 0.48 g was powdered. About 100 mg of the latter were used for bulk rock analyses. Major elements (Ti, Al, Cr, Fe, Mn, Mg, Ca, Na, K, and P) were determined by ICP-AES (inductively coupled plasma-atomic emission spectrometry) using the procedure described by Cotten et al. (1995). The accuracy of this system is better than 5%, and the reproducibility better than 3%. Trace element concentrations were measured by ICP-MS (inductively coupled plasma-mass spectrometry) using a Thermo Element 2 spectrometer following the procedure described by Barrat et al. (2007). Based on standard measurements and sample duplicates, trace element concentration reproducibility is generally better than 5%, except for W, which is generally better than 10%.

Trace element abundances of pyroxenes and plagioclases in NWA 5073 were determined by laser ablation-inductively coupled plasma-mass spectrometry (LA-ICP-MS) at the Institut Universitaire Européen de la Mer, Plouzané. The analyses were performed under a He atmosphere

using an ArF-Excimer (193 nm wavelength) laser ablation system (Geolas Pro102), connected to a Finnigan Thermo Element 2 spectrometer. Concentrations were determined on individual spots using a 60 μm-diameter laser beam and a laser repetition rate of 10 Hz. Background and peak were measured for 40 s and 210 s, respectively. For all data, NIST 612 and BCR-2G glass standards were both used for external calibration of relative element sensitivities, using values given by Jochum et al. (2005). Replicate analyses of the USGS basaltic-glass standard BIR-1G run at intervals during the analytical session, yielded an external reproducibility generally better than 5% (1σ relative standard deviation). Analytical and data reduction procedures followed those described by Barrat et al. (2009). Results were normalized to CaO abundances measured by electron microprobe as an internal standard to account for variable ablation yield.

Oxygen isotope analysis was carried out at the Open University using an infrared laser fluorination system (Miller et al., 1999). A 2 mg aliquot of NWA 5073, taken from a larger batch of homogenized powdered sample material (~100 mg), was loaded in the sample chamber, together with various international and internal oxygen isotope standards. To maximize yields and decrease the risk of cross contamination, the powdered sample and standards were fused in vacuum to form a glass bead prior to fluorination. O_2 was liberated by heating the glass beads using an infrared CO_2 laser (10.6 μm) in the presence of 210 torr of BrF_5. After fluorination, the O_2 released was purified by passing it through two cryogenic nitrogen traps and over a bed of heated KBr. O_2 was analyzed using a Micromass Prism III dual inlet mass spectrometer. Published system precision (1σ) (Miller et al., 1999), based on replicate analyses of international (NBS-28 quartz, UWG-2 garnet) and internal standards, is approximately ±0.04‰ for $\delta^{17}O$, ±0.08‰ for $\delta^{18}O$, and ±0.02‰ for $\Delta^{17}O$. Oxygen isotope analyses are reported in standard δ-notation where $\delta^{18}O$ has been calculated as:

$$\delta^{18}O = ((\delta^{18}O/\delta^{16}O)_{sample}/(\delta^{18}O/\delta^{16}O)_{ref}) - 1) \times 1000 \quad (2)$$

and similarly for $\delta^{17}O$ using $^{17}O/^{16}O$ ratio. $\Delta^{17}O$ has been calculated using the linearized format of Miller (2002):

$$\Delta^{17}O = 1000 \ln (1 + (\delta^{17}O/1000)) - \lambda\, 1000 \ln (1 + (\delta^{18}O/1000)) \quad (3)$$

with $\lambda = 0.5247$.

Results

Mineralogy

Northwest Africa 5073 is a desert find with a total mass of 185 g, representing an unequilibrated, mesostasis-rich basaltic eucrite with the coarsest subophitic to slightly variolitic (fan-spherulitic) texture among the known eucrites. It is an unbrecciated rock that preserved its crystallization texture. It is mainly composed of elongated, unequilibrated pyroxene crystals up to 1.2 cm and plagioclase laths up to 0.3 cm in length (Fig. 1). Large phenocrysts of pyroxene make up approximately 25 vol.% of the whole rock (Table 1). In variolitic areas, the plagioclase tends to be skeletal, i.e., it occurs as partly hollow crystals, which is indicative of rapid cooling. Euhedral

chromite grains, occasionally dendritic, frequently occur with grain sizes up to 0.8 mm. Their chemical composition (Table 2) is in the range of those for the unequilibrated eucrite Pasamonte (Mittlefehldt et al., 1998). Fine-grained areas (mesostasis) that make up about 8.5 vol.% of the rock, occur interstitially to the large crystals (Figs. 1 and 3). Terrestrial weathering of the sample is indicated by the breakdown of about half of the metals and the occurrence of calcite, and Ba-sulfates in some cracks all over the thin section. According to the scheme proposed for chondrites by Wlotzka (1993), NWA 5073 is moderately weathered (W2-3).

Large pyroxene crystals are chemically unequilibrated with cores of $En_{51-60}Fs_{34-5}Wo_{2-8}$ and rims of $En_{20-34}Fs_{42-63}Wo_{8-34}$ (Figs. 2 and 3; Table 2). The pyroxene composition depicted in Fig. 2, reflects magmatic zoning from Mg-rich cores to Fe-rich rims of large pigeonite laths adjacent to surrounding plagioclase crystals, which is typical of more rapidly cooled basalts containing pyroxene that has not exsolved on a µm scale, e.g., Y-75011 (Takeda et al., 1994). As emphasized by e.g., Takeda et al. (1982), chemical zoning in pyroxene primarily depends on the bulk chemistry of the basaltic melt and on crystal-growth conditions such as the degree of supercooling and nucleation. Re-equilibration of chemical zoning in pyroxene crystals did not occur in our sample. Thus, NWA 5073 was not formed in a slow cooling environment, as indicated by the skeletal nature of plagioclases, (see Fig. 3a), and was not affected by a long-term, high-temperature event, which would have resulted in re-equilibration of pyroxene crystals. The large pyroxene crystals are frequently twinned and fractured mainly perpendicular to the c-axis. This is in strong contrast to the adjacent plagioclase crystals which do not show this fracturing. The small pyroxenes interstitial to the large crystals show similar Ca contents as the rims of large crystals, but contain somewhat more Fe (Fig. 2, open squares, Table 2).

Occasionally, very thin (<1µm) exsolution lamellae of augite in the host pyroxenes can be observed (e.g., Fig. 3). Pyroxenes in contact with the mesostasis frequently have a corroded appearance. Large pyroxene grains are crosscut by fractures that are mainly filled by Fe-rich olivine. Originating from these veins, a distinct Fe-enrichment of the adjacent host pigeonite can be observed, which clearly parallels the veins (Fig. 3). Pyroxene areas distant to these veins appear as Mg-rich “cores”, surrounded by Fe-enriched areas. These “cores” seem to have preserved their original composition from primary crystallization ($Fs_{\sim 34}$). Additionally, Fe has effectively diffused from the olivine veins and larger fractures devoid of olivine veins into the host pyroxene crystals along certain crystallographic orientations, which probably represent cleavage plans (see Figs. 3d and 4a-b). Veins of Fe-rich olivine (Fa_{65-71}) are clearly restricted to the large pyroxene crystals and always end abruptly at their boundaries. These veins are very irregular with distinct thickness variations (Fig. 3a-c). The olivine appears to have grown along preexisting fractures of its host pyroxene, while adjacent large plagioclase crystals are devoid of it (Fig. 3a-c). Euhedral chromite, and troilite crystals, and sporadic subrounded apatite grains occur within these veins (Fig. 3d). Similar olivine veins have been described from a few other eucrites and howardites, namely Macibini, Y-7308, Y-790260, Y-75011, Y-82202,

NWA 049, NWA 1000, and NWA 2061 (Takeda and Yanai, 1982; Takeda et al., 1983; Metzler, 1985; Warren, 2002; Barrat et al., 2011).

Two primary feldspar generations occur, namely large plagioclase laths (up to 3 mm in length) and small plagioclase grains located in the mesostasis, both of which are compositionally in the typical eucrite range (e.g., Mittlefehldt et al., 1998) of $An_{76-92}Ab_{8-22}Or_{0-3}$ (Fig. 5; Table 2). The plagioclases found in mesostasis areas tend to be more Ab-rich compared to large plagioclase laths (Fig.5). Many large plagioclase crystals are clouded by myriads of exsolved tiny pyroxene and SiO_2 grains, as commonly observed in eucrites (e.g., Harlow and Klimentidis, 1980; Metzler et al., 1995). Additional to the primary plagioclases, we identified another, probably second generation of feldspars that are typically An_{97-100} in composition (Fig. 5) and were usually found in association with Fe-rich olivine veins within large pyroxene laths (Fig. 4).

The mesostasis consists of tridymite laths up to 0.8 mm, Ni-poor metallic Fe (<300 μm), ilmenite (<60 μm), chromite, plagioclase, augite, apatite, merrillite, troilite, zircon, baddeleyite, and very small amounts of Fe-rich olivine. In addition, sporadic anorthite (An_{95}) was found. In some cases the mesostasis areas are not well-defined and appear blurred. More than 30 grains of Zr-bearing phases, such as zircon, baddeleyite, and zirconolite grains, with diameters ranging from 1 to 30 μm were found in the mesostasis (Fig. 6; Roszjar et al., 2009b). They are typically located interstitial to ilmenite, pyroxene, plagioclase, and iron metal, and/or occur as inclusions in ilmenite and are subhedral to anhedral, and rounded in shape. The major element composition is consistent for all analyzed zircon grains (see Table 2), and within the range of prior published data on eucrite zircon grains (Saiki et al., 1990; Bukovanská et al., 1991; Ireland and Bukovanská, 1992; Yamaguchi et al., 2001; Yamaguchi and Misawa 2001; Misawa et al., 2005; Barrat et al., 2007; Roszjar et al., 2009c). In addition to BSE images that were taken for all selected zircon grains, cathodoluminescence images were exemplarily taken for some of them. Here it was found that the luminescence behavior is distinct from grain to grain. Nevertheless, some zircon grains are characterized by partial luminescence with a preferred direction, increasing towards the edges of the grains, also giving evidence for a thermal reaction front caused by a metamorphic event (Fig. 6).

Shock features

Northwest Africa 5073 as a whole is very weakly shocked, possibly equivalent to a S2 stage as defined for chondrites (Stöffler et al., 1991; Bischoff and Stöffler, 1992). Evidence for shock is given by the undulatory extinction of about half of the plagioclases and the occurrence of dislocation lines in large pyroxene laths.

There is also evidence for an earlier shock event which affected this meteorite prior to annealing during thermal metamorphism. Minor tiny, euhedral to subhedral troilite (FeS) grains and blebs of metallic Fe-Ni that are usually <3 μm, occur within the plagioclase crystals and are arranged in curvilinear trails, frequently aligned in a pearl chain manner, which do not follow the cleavage planes and are restricted to the interiors of individual silicate crystals. It is known that metal and sulfide are

readily mobilized and re-precipitated in the shape of trails during shock metamorphism (Rubin, 1992). These inclusions are in principle the cause of the silicate darkening which can be described as impact-generated "shock darkening" (Rubin, 1992; Dodd, 1981). After annealing the metal and sulfide veins are probably transformed to the tiny blebs described above.

Bulk chemical composition

The major and trace element abundances of NWA 5073 share similarities with other Stannern-trend eucrites, such as Bouvante and Stannern (Table 3). Northwest Africa 5073 has respectively FeO_{total}/MgO ratio (2.31) and Sc concentration (25.8 µg/g) slightly lower, and MgO (8.70 wt%), Cr_2O_3 (0.59 wt%) concentrations higher to that of typical Main Group eucrites (e.g., Warren et al., 2009). Similar "high" MgO abundances were previously measured on Pomozdino by Warren et al. (1990), and led these authors to propose that this meteorite could be a partial cumulate. Moreover, an increase of MgO can be produced by a slight oversampling of pyroxene in the powdered sample. Because NWA 5073 is unequilibrated, these two possibilities can be easily discussed. We have calculated the apparent distribution coefficient between the pigeonite cores (with n = 27) and the whole rock composition ($K_D^{Fe/Mg} = (Fe/Mg)_{pigeonite\ core}/(Fe/Mg)_{whole\ rock}$). The result, $K_D^{Fe/Mg} = 0.32 \pm 0.01$ (2σ), is in very good agreement with experimental distribution coefficients obtained for eucritic systems ($K_D^{Fe/Mg} = 0.30$; Stolper, 1977). A lower value would have been obtained if the powder contained a pyroxene excess. Thus, the pigeonite cores formed from a parental melt displaying the same Fe/Mg as the analyzed powder. We conclude that the whole rock composition is probably close to its parental melt. However, we suspect that the rather high Cr_2O_3 abundance is an artifact produced by a very small excess of chromite in the powder.

Weathered meteorite finds from the Sahara generally exhibit marked Ba and Sr enrichments that are sensitive indicators for the development of secondary phases (e.g., Stelzner et al., 1999; Barrat et al., 2003; Crozaz et al., 2003). NWA 5073 is no exception, and displays high Ba and Sr concentrations (177 µg/g and 2131 µg/g, respectively). It should be noted that its Th/U ratio (=3.38) and Pb abundances (= 0.24 µg/g), which are other possible indicators of weathering, do not show perturbed values.

Although NWA 5073 is characterized by a low FeO/MgO ratio (Fig. 7, Table 3), it displays high levels of concentrations for incompatible elements, as exemplified by the REEs (Fig. 8). This suggests that NWA 5073 is a new member of the Stannern-trend eucrites, transitional between the Main Group and the REE-rich eucrites such as Stannern or Bouvante. Indeed, NWA 5073 exhibits a much more pronounced negative Eu anomaly (Eu/Eu*=0.68) and a higher Gd/Lu ratio than a regular Main Group or Nuevo Laredo eucrite, and its REE-pattern is parallel to those of the Stannern-trend eucrites (e.g., Bouvante and Stannern). These similarities extend to other incompatible trace element abundances, and, interestingly, NWA 5073 displays a marked negative Be anomaly (Fig. 9) which is a distinctive feature of the Stannern-trend eucrites (Barrat et al., 2007). Thus, we can deduce that NWA 5073 is clearly a new member of this rare group of eucrites.

Mineral chemical composition

In addition to bulk rock trace elements, REE concentrations of pyroxenes and plagioclases have been determined with LA-ICP-MS. Results are shown in Table 4. CI normalized REE patterns for pyroxenes and plagioclases are presented in Fig. 10. In eucrites, pyroxene is one of the dominant phases next to plagioclase, and a sensitive indicator of intrinsic variables such as oxygen fugacity and temperature that may affect their crystallization sequence. Therefore, major, minor, and trace elements have been investigated in order to decipher the evolution of the NWA 5073 meteorite. Rare earth element abundances of selected pyroxene cores in NWA 5073 are in the range of 0.02× (La) to 2.2× (Lu) CI chondritic abundances, relative to the values given in Evensen et al. (1978), which is within the range presented by Pun and Papike (1996). All analyzed pigeonite cores in NWA 5073 exhibit variable REE abundances that correlate with Ca concentrations, and are generally HREE-enriched with a pronounced negative Eu anomaly (Eu/Eu*=0.68). A total of 7 plagioclase grains have been analyzed for their REE abundances. The latter exhibit a pronounced positive Eu anomaly with Eu/Eu* = 61, thus are in agreement with the data range for eucrites previously reported in literature (e.g., Hsu and Crozaz, 1996; Floss et al., 2000). The REE patterns of single plagioclases are slightly fractionated with LREE being enriched. The total abundance of REE ranges from 2× (La) to 0.1 (Er) × CI (Evensen et al., 1978), except for Eu (Table 4).

Oxygen isotope composition

The oxygen isotope composition of NWA 5073 obtained in this study ($\delta^{17}O$ = 1.89 ‰, $\delta^{18}O$ = 4.05 ‰, $\Delta^{17}O$ = -0.24 ‰) is plotted in Fig. 11 along with the data for other HED samples obtained by Greenwood et al. (2005). The $\Delta^{17}O$ value for NWA 5073 is close to the average HED value of -0.239 ± 0.007 (1σ) obtained by Greenwood et al. (2005) and indicates that the meteorite is a normal member of the HED suite (Roszjar et al., 2009a). NWA 5073 was not acid leached prior to oxygen isotope analysis and has a slightly elevated $\delta^{18}O$ value compared to the eucrites analyzed by Greenwood et al. (2005), which may reflect a small degree of terrestrial weathering. However, the $\delta^{18}O$ composition of NWA 5073 is within the range obtained by Wiechert et al. (2004), which extends to $\delta^{18}O$ values of 4.5‰.

Structural state of zircon grains as obtained by Raman spectroscopy

It has been demonstrated that micro-Raman spectroscopy is a powerful tool to quantify the degree of self-irradiation damage in single zircon grains caused by the radioactive decay of incorporated U and Th (metamictization) as well as the structural recovery by thermal annealing (Nasdala et al., 1995, 1998, 2001; Wopenka et al., 1996; Zhang et al., 2000a- c; Geisler et al., 2001; Geisler, 2002; Palenik et al., 2003). As already mentioned, the $\nu_3(SiO_4)$ band, reflecting antisymmetric Si-O stretching motions of the SiO_4 tetrahedra, is particularly sensitive to structural changes associated with self-irradiation. Raman measurements of zircon grains in sample NWA 5073 reveal a decreased frequency and an increased broadening of the $\nu_3(SiO_4)$ band with increasing radiation dose (*D*; Fig. 12*)* as calculated from the U and Th concentration measured by EPMA and an inferred age of 4.55 Ga

(Table 5). The frequency shift is attributed to an increase in interatomic distances, i.e., to a slight expansion of the lattice of the crystalline domains, whereas the increase in linewidths is attributed to the fact that the distribution of bond lengths and bond angles within and between SiO_4 tetrahedra becomes increasingly irregular (Wopenka et al., 1996).

In the diagram linewidth (given as FWHM) vs. frequency of the $\nu_3(SiO_4)$ band all measurements plot along the radiation damage trend (*RDT*; Fig. 13a) that is mainly defined by measurements from variably self-irradiation-damaged, alluvial zircons from Sri Lanka (Geisler et al., 2001). Dry annealing experiments with self-irradiation-damaged zircon revealed that episodically annealed samples plot above the RDT (arrows in Fig. 13a). A comparison of Raman data from natural zircons with experimental annealing trends thus allows recognizing episodically annealed zircons, provided that post-annealing radiation damage did not completely obscure the annealing effect, i.e., did not push the data points back to the RDT in the frequency versus linewidth diagram shown in Fig. 13a. This means that most likely only relatively recent episodic annealing events are recognizable in this diagram. However, the observed congruency with the RDT does not imply that the NWA 5073 zircons were not annealed during their history. In fact, from the diagram linewidth of the $\nu_3(SiO_4)$ band vs. α-decay dose (*D*; Fig.13b) it can be observed that all analyzed zircon grains from the NWA 5073 eucrite plot consistently below the so-called damage accumulation curve, defined by Palenik et al. (2003). Samples that have been neither episodically nor continuously annealed during their geological history (i.e., that have accumulated the entire damage over their geologic history) should plot, within errors, onto this accumulation trend. The observation that most of the measurements from zircon grains of sample NWA 5073 plot significantly below this curve is unambiguous evidence that they were thermally annealed (Palenik et al., 2003), either continuously for a prolonged period of time or episodically as a result of a short time heating event. In the latter case, however, the heating event must have occurred very early in their history.

Discussion

Most HED meteorites show textural and chemical evidence for extensive thermal annealing after crystallization such as: Fe-Mg equilibration in pyroxenes, exsolution of Ca-pyroxenes within host pigeonites, plagioclase and pyroxene clouding, and recrystallization of lithic clasts and clastic matrices (e.g., Duke and Silver, 1967; Mason et al., 1979; Takeda and Graham, 1991; Metzler et al., 1995; Yamaguchi et al., 1996; Bogard and Garrison, 2003; Llorca et al., 2009). Moreover, many eucrites were brecciated and reheated by impacts (e.g., Metzler et al., 1995; Bogard and Garrison, 2003). In the case of NWA 5073, the thermal history seems to be very complex. In the following, we discuss possible scenarios to explain both chemical and textural characteristics of this sample.

Formation of primary phases in a magma chamber and excavation

Since NWA 5073 is a coarse-grained basaltic sample containing large, elongated pyroxene crystals that preserved their igneous Mg-Fe zoning, we can infer that this sample derived from a relatively fast cooling magma source. However, due to the texture and the composition of the crystals (e.g., Al content), the cooling rate must have been slower than 1 °C/hour (Walker et al., 1978; Powell et al., 1980). Large pyroxene laths might represent an early crystallized phase from a magma that experienced fast excavation during volcanic eruption. The process of fast excavation is affiliated to thermal and pressure relief that caused mechanical stress in preexisting pyroxene crystals, probably leading to fracturing and bending of the crystals. A fast excavation of the magma onto the surface of the parent body results in quenching of the melt. Thus, this explains the observed skeletal, and seemingly cotectic crystallisation of silicates (pyroxenes and plagioclases) and other minor phases, while leaving the large previously crystallized pyroxene crystals relatively unaffected.

Episode of secondary annealing and rapid cooling

Several mineralogical and chemical observations clearly indicate an episode of thermal annealing that caused disturbance of the NWA 5073 sample: (1) disturbance of the Lu-Hf system, as demonstrated by Roszjar and Scherer (2010), (2) Fe-diffusion along cracks and cleavage planes within the zoned pyroxene crystals (Fig. 3b-d), and (3) recovery of the crystal structure of zircon grains (Fig. 13b). Based on these observations, it is possible to constrain the time-temperature conditions of the reheating event which is discussed in the following.

The observation of Roszjar and Scherer (2010) that about half of the mineral fractions, mainly pyroxene-rich fractions and the whole rock, form an isochron of 4.68 ± 0.14 (2σ) Ga, whereas the other half, e.g., chromite, metal, plagioclase-rich fractions, define a secondary isochron of 4.31 ± 0.14 (2σ) Ga, is clear evidence that the Lu-Hf system in some minerals was disturbed. Since the time gap between the primary crystallisation of the eucrite and the event that disturbed the Lu-Hf system is at least ~370 Ma, thermal metamorphism, driven by internal heat on the parent body, can be ruled out as the cause for the isotope resetting. On the contrary, it is rather likely that the thermal event was short and intensive. This is supported be the observations that (i) the primary pyroxenes preserved their initial magmatic Mg-Fe-Ca zoning, (ii) the exsolution lamellae of augite in the host pyroxene grains are very thin (<1μm), (iii) and the mesostasis shows a fine-grained subophitic texture. A short, but intense heating event more than 300 Ma after the primary crystallization of the eucrite is only conceivable by a shock-triggered process, e.g., by a superheated impact melt produced by a large impact. The impact melt could have been injected into neighbouring target rock lithologies, causing a short thermal pulse followed by fast cooling. Fast cooling is indicated by the absence of recrystallization textures, which have neither been observed in the coarse mineral grains nor in the fine-grained mesostasis. As discussed by Yamaguchi and Mikouchi (2005) small fractions of melt can be formed when a eucrite is heated to a temperature slightly above its solidus of about 1100°C (Stolper, 1977) for a short period of time. However, a temperature above the solidus would have

caused re-melting of mesostasis components, and a depletion of light rare earth elements (LREE) of the whole rock, which has not been observed (Fig. 8). This suggests that the NWA 5073 sample was in fact reheated to a certain degree for a short period of time, but most likely not re-melted. The absence of any evidence for partial re-melting constrains the maximum annealing temperature to about 1100°C.

Assuming a maximum reheating temperature of 1100°C and that the reheating process possibly also triggered Fe-diffusion along cracks and cleavage planes in large pyroxenes (Fig. 3d), the duration of the heating event can now be estimated from the relation $L_D = 2\sqrt{Dt}$, where L_D is the diffusion length, D the diffusion coefficient for Fe-diffusion in pyroxene, and t the diffusion time. From BSE images (e.g., Fig. 3d), we measured an average diffusion path length, L_D, of about 25 µm for Fe-diffusion between the Fe-rich olivine veins into the pyroxene. Using published diffusion coefficients for Fe-Mg diffusion in pyroxene (Freer, 1981; Cherniak and Dimanov, 2010; Ganguly and Tazzoli, 1994), we estimated that the heating to a temperature of about ~1100°C could have only lasted for some hours (5 hours at most). This order of magnitude for the duration of the reheating event obtained from this back-of-the-envelope calculation is also consistent with the observation that the pigeonite pyroxenes still show chemical zoning, i.e., were not re-equilibrated. It is noted that the order of magnitude of hours would also hold for slightly longer diffusion lengths and slightly lower temperatures.

Probably the most convincing evidence for a secondary heating event is given by the Raman measurements of ten zircon grains. In the plot of the linewidth of the $\nu_3(SiO_4)$ stretching band near 1008 cm^{-1}, expressed as the full width at half maximum (FWHM), versus the calculated radiation dose of a single zircon grain (D), most analyzed points plot below the radiation damage accumulation curve (Fig. 13b). We recall that samples that have neither been episodically nor continuously annealed during their geological history and accumulated the entire structural damage should plot on this curve. Laboratory dry annealing experiments with radiation-damaged zircon revealed that the temperature and duration of a thermal event determines the degree of structural recovery that occurs after a certain degree of structural damage has been accumulated, i.e., during an episodic annealing event (Geisler et al., 2001; Geisler, 2002). Considering the low U and Th concentrations measured today, the zircons accumulated only a limited amount of radiation damage during the first 370 Ma after their crystallisation in the eucrite melt. Experimental work has shown that significant structural recovery of less self-irradiation-damaged samples within time scales of a few hours only occurs at temperature in excess of about 900°C (Geisler et al., 2001; Zhang et al., 2000b; Geisler, 2002). It is thus likely that the actual temperature of the event affecting the NWA 5073 eucrite was between 900 and 1100°C.

Formation of olivine-rich veins

The occurrence of veins composed of Fe-rich olivine, secondary plagioclase, and small troilite and chromite grains inside these veins within large pyroxene phenocrysts (Fig. 3) requires careful consideration, especially as recent papers have suggested that minerals in these veins might have

crystallized from fluids or gases during a metasomatic reaction (Barrat et al., 2011). At this point we would like to make very clear that the authors have rather different views concerning the formation of the olivine-rich veins within the cores of pyroxene. Thus, we try to unravel the origin of the olivine-rich veins in NWA 5073, suggesting two valid possible mechanisms of formation that will be discussed separately in the following paragraphs:

(a) ***Formation of the olivine-rich veins in NWA 5073 by metasomatism***

Based on distinct mineralogical features in eucrites, Barrat et al. (2011) defined a three-type classification scheme for secondary alteration. The first type is characterized by Fe-enrichment along cracks that cross cut large pyroxene crystals, and by occasional occurrence of Fe-rich olivine in some fractures (e.g., Pasamonte). The second type reveals involves deposits of Fe-rich olivine (Fa_{64-86}) and minor amounts of troilite inside the cracks as well as the sporadic occurrence of secondary Ca-rich plagioclase (An_{97-98}) associated with Fe-rich olivine (NWA 2061, Y-75011, and Y-82202). The third type is identifiable by a more frequent occurrence of Ca-rich secondary plagioclase, partial fillings of cracks or rims of primary plagioclases with small crystals of secondary plagioclase, and Fe-enrichment of pyroxenes accompanied by significantly decreased Al contents (NWA 049; Barrat et al., 2011). According to this scheme, NWA 5073 belongs to the second type, as it contains secondary plagioclase (An_{97-100}) associated with Fe-rich olivine veins, typically located at the grain boundaries between larger primary plagioclase and large pyroxene laths. Based on these observations, Barrat et al. (2011) proposed that Fe-rich olivine veins may be secondary precipitation products formed by the interaction between pyroxene crystals and Fe-rich gas or fluid phases that invaded the pyroxene crystals along fractures and offset planes. The chemical composition of the metasomatic agent is at present not well constrained but could have been aqueous (Barrat et al., 2011).

(b) Formation of the olivine-rich veins in NWA 5073 by incongruent melting

The large pyroxene crystals contain olivine-rich veins that abruptly end at their margins (Fig. 3a-c). The Fe-rich olivine within these veins is accompanied by An-rich plagioclase, and small Cr-rich oxides (chromites) and troilites. As shown in Fig. 3, all other adjacent silicate phases (small pyroxenes and large plagioclases) are devoid of these veins. We believe that the chromites may be of genetic significance, as it is known that the solubility of Cr^{3+} in silicate melts is rather high and Cr^{3+} is immobile in hydrous fluids (e.g., Roeder and Reynolds, 1991). Thus, mobilization and precipitation of small chromite grains in the olivine-rich veins found in NWA 5073 seems to indicate a magmatic albeit secondary origin. As an alternative to the arguments presented in the previous paragraph, it may have been that veins of olivine, anorthite, and Cr-rich oxides were formed by incongruent *in-situ* melting of pyroxene ($Fs_{34}Wo_2$) at a temperature slightly above the temperature of formation of primary, Mg-rich pigeonites, i.e. at about 1150°C (Stolper, 1977). This is suggested to have taken place during a short period of a small temperature excursion in the magma chamber. The process of

incongruent melting must have taken place after formation of primary pyroxenes in the magma chamber, but prior to excavation of the sample. During this peritectic reaction, olivine forms and the remaining melt crystallizes minor, extremely Ca-rich plagioclase. A similar process of incongruent melting of pigeonites producing olivine (Fo_{35-55}) plus silica was experimentally shown by e.g., Huebner et al. (1973) and Huebner and Turnock (1980). It should be noted that the experimental data confirm that the olivines in the veins (Fa_{65-71}) are in equilibrium with the outer rims of large pyroxene grains and the small pyroxenes (~Fs_{62-68}; Table 2). Since the pyroxene, which melts incongruently, does not contain significant Na, the crystallizing plagioclase has to be low in Na and, consequently, extremely rich in Ca (An_{97-100}). Cr- and S-rich oxides that are found within the olivine-rich veins are sometimes also located within the primary pyroxenes. The incongruent melting of pigeonite requires only a few tens of degrees above the peritectic temperature, so that if we employ the aforementioned experimental data we estimate some 1150°C for the formation of the olivine veins in this scenario.

In summary, it seems that both interpretations for the formation of olivine-rich veins in large pyroxenes, as discussed above, have some inconsistencies which cannot be resolved at this point. The metasomatism model cannot fully explain the occurrence of Fe-rich olivine veins in large pyroxene phenocrysts, while the adjacent silicate phases (small pyroxenes and large plagioclases) are devoid of them. Furthermore, the occurrence of chromite within these veins is hardly explained by metasomatic fluids. On the other hand, the model which involves incongruent melting cannot readily explain certain textural observations, such as the only minor occurrence of olivine-rich veins in contact with plagioclase. To unravel the process which leads to the formation of such Fe-rich olivine veins in large pyroxenes, one would need further oxygen isotope data of these veins. Furthermore, more realistic melting experiments on bulk eucrite samples and pyroxenes would be helpful.

Pairing or launch-pairing of some Stannern-trend eucrites?

According to sample textures, grain sizes, including the occurrence of Fe-rich olivine veins in large pyroxenes and secondary plagioclases, NWA 5073 resembles some other Stannern-trend eucrite finds from the Sahara, namely NWA 1000 and NWA 2061. Since the occurrence of Fe-rich olivine veins in large pyroxene crystals is not restricted to the NWA 5073 sample, but was also found to occur in other eucrites and howardites, namely Y-7308, Y-790260, Y-75011, and NWA 1000, Macibini, and NWA 2061 (Takeda and Yanai, 1982; Takeda et al., 1983; Metzler, 1985; Warren, 2002; Barrat et al., 2007; and Barrat, unpublished data), one can argue that these findings give some evidence for a large-scale but certainly not global parent body process. However, NWA 1000 is severely shocked (S4), as documented by the transformation of half of the plagioclase into maskelynite (Warren, 2002). Thus, NWA 5073 and NWA 1000 are certainly not fall-paired. Since NWA 2061 is as REE-rich as Stannern and thus distinct to NWA 5073, a pairing between those eucrites and NWA 5073 seems unlikely. However a certain pairing, especially for the Stannern-trend eucrite finds with the NWA 5073 sample,

615 can only be unequivocally proven by obtaining noble gas exposure ages. However, some of these
616 samples may be launch-paired.
617
618 **Summary and Conclusions**
619 In summary, our results are: (i) Northwest Africa 5073 is a coarse-grained basaltic,
620 unequilibrated, and non-brecciated eucrite with a subophitic to slightly variolitic (fan-spherulitic)
621 texture, mainly composed of small equilibrated pyroxenes (~40 vol.%), elongated, unequilibrated
622 pyroxene phenocrysts up to 1.2 cm (~ 25 vol.%), plagioclase laths up to 0.3 cm in apparent length
623 (~26 vol. %), and about 8.5 vol.% mesostasis. (ii) This sample is very weakly shocked and moderately
624 weathered (W2-3). (iii) Based on its oxygen isotope composition ($\delta^{17}O$ = 1.88 ‰, $\delta^{18}O$ = 4.05 ‰,
625 $\Delta^{17}O$ = -0.239 ‰), we can deduce that NWA 5073 is a normal member of the HED suite of
626 achondrites. (iv) The large unequilibrated pyroxenes preserved their initial magmatic Mg-Fe-Ca
627 zoning and are crosscut by olivine-rich veins (Fa_{65-71}) which are restricted to them. These veins also
628 contain minor chromite, troilite, and very Ca-rich plagioclase. (v) Three different plagioclase
629 generations occur: (a) large primary plagioclases crystals ($An_{76-92}Ab_{8-22}Or_{0-3}$), (b) small primary
630 plagioclase grains of similar composition as the large ones that are concentrated in mesostasis areas
631 and, (c) a secondary generation of small plagioclases (An_{97-100}), typically 5-20 μm in diameter, always
632 found in association with Fe-rich olivine veins. (vi) Due to the occurrence of these olivine-rich veins
633 in large pyroxene crystals and the sporadic occurrence of secondary plagioclase associated with the
634 former, NWA 5073 belongs to stage 2-type eucrites, according to the classification scheme for
635 secondary alteration as proposed by Barrat et al. (2011). Other members of this group include NWA
636 2061, Y-75001, Y-82202, and probably NWA 1000 (Barrat et al., 2011). (vii) Based on its bulk
637 chemical composition (e.g., high Ti with TiO_2 = 0.77 wt.%, La = 4.18 μg/g, negative Be anomaly),
638 NWA 5073 displays a distinctive Stannern-trend signature. (viii) The REE pattern of NWA 5073 bulk
639 rock, which is characterized by flat LREE and a slight HREE-depletion (La_n/Yb_n=1.38) with a
640 pronounced negative Eu anomaly (Eu/Eu*=0.68), resembles those of other Stannern-trend eucrites.
641 (ix) Northwest Africa 5073 contains zircon grains up to 30 μm in size that were invariably found in
642 the mesostasis. These zircon grains are metamict and were annealed, indicating a short high-
643 temperature event (probably induced by shock) occurring after primary crystallization of main sample
644 constituents. (x) A short but intense heating event that caused disturbance of the sample is also
645 indicated by the disturbance of the Lu-Hf system, and Fe-diffusion along cracks and cleavage planes
646 within unequilibrated pyroxene crystals. (xi) According to sample textures, grain sizes, and the degree
647 of alteration, including the occurrence of olivine-rich veins in large pyroxenes, as well as secondary
648 plagioclases, NWA 5073 resembles some other Stannern-trend eucrite finds from the Sahara, namely
649 NWA 1000, NWA 2061 and NWA 4523. However, these four samples are unlikely fall-paired as
650 discussed above.
651

Acknowledgements

The authors are grateful to A. Yamaguchi and an anonymous reviewer for their helpful reviews, which helped improving the paper and A. Ruzicka for thoughtful comments and for handling this article. We also thank U. Heitmann for sample preparation, C. Bollinger for assistance at the LA-ICP-MS, J. Berndt for guidance with the electron microprobe, and M. Menneken for help with Raman measurements. This study was partially supported by the German Research Foundation (DFG; grant Bi 344/9-1) and T. Geisler acknowledges a Heisenberg scholarship from the DFG.

References

Åmli R. and Griffin W. L. 1975. Microprobe analysis of REE minerals using empirical correction factors. *American Mineralogist* 60:599-606.

Armstrong J. T. 1991. Quantitative elemental analysis of individual microparticles with electron beam instruments. *Electron Probe Quantitation,* edited by Heinrich K. F. J. and Newbury D. E. New York: Plenum Press. pp. 261-315.

Barrat J. A., Blichert-Toft J., Gillet Ph. and Keller F. 2000. The differentiation of eucrites: the role of in-situ crystallization. *Meteoritics & Planetary Science* 35:1087-1100.

Barrat J. A., Jambon A., Bohn M., Blichert-Toft J., Sautter V., Göpel C., Gillet Ph., Boudouma O. and Keller F. 2003. Petrology and geochemistry of the unbrecciatted achondrite North West Africa 1240 (NWA 1240): an HED parent body impact melt. *Geochimica et Cosmochimica Acta* 67:3959-3970.

Barrat J. A., Yamaguchi A., Greenwood R. C., Bohn M., Cotten J., Benoit M., and Franchi I. A. 2007. The Stannern trend eucrites: contamination of main group eucritic magmas by crustal partial melts. *Geochimica et Cosmochimica Acta* 71:4108-4124.

Barrat J. A., Yamaguchi A., Benoit M., Cotten J. and Bohn M. 2008. Geochemistry of diogenites: Still more 392 diversity in their parental melts. *Meteoritics & Planetary Science* 43:1759-1775.

Barrat J. A., Yamaguchi A., Greenwood R. C., Bollinger C., Bohn M., and Franchi I. A. 2009. Trace element geochemistry of K-rich impact spherules from howardites. *Geochimica et Cosmochimica Acta* 73:5944-5958.

Barrat J.A., Yamaguchi A., Zanda B., Bollinger C., Bohn M. (2010) Relative chronology of crust formation on asteroid 4-Vesta: Insights from the geochemistry of diogenites. *Geochimica et Cosmochimica Acta* 74:6218-6231.

Barrat J. A., Yamaguchi A., Bunch T. E., Bohn M., Bollinger C., and Ceuleneer G. 2011. Possible fluid-rock interactions on differentiated asteroids recorded in eucrite eucritic meteorites. *Geochimica et Cosmochimica Acta* 75:3839-3852.

Beck A. W. and McSween H. Y. Jr. 2010. Diogenites as polymict breccias composed of orthopyroxenite and harzburgite. *Meteoritics & Planetary Science* 45:850-872.

Binzel R. P. and Xu S. 1993. Chips off of Asteroid 4 Vesta: Evidence for the parent body of basaltic achondrite meteorites. *Science* 260:186-191.

Bischoff A. and Stöffler D. 1992. Shock metamorphism as a fundamental process in the evolution of planetary bodies: Information from meteorites. *European Journal of Mineralogy* 4:707-755.

Bischoff A., Scott E. R. D., Metzler K., and Goodrich C. A. 2006. Nature and origins of meteoritic breccias. *Meteorites and the early solar system II*, edited by Lauretta D.S. and McSween H.Y. Tucson: The University of Arizona Press. pp 679-712.

Bland P. A., Spurný P., Towner M. C., Bevan A. W. R., Singleton A. T., Bottke W.F. Jr., Greenwood R. C., Chesley S. R., Shrbený L., Borovička J., Ceplecha Z., McClafferty T. P., Vaughan D., Benedix G. K., Deacon G., Howard K. T., Franchi I. A., Hough R. M. 2009. An anomalous basaltic meteorite from the innermost main belt. *Science* 325:1525-1527.

Bogard D. and Garrison D. 2003. ^{39}Ar-^{40}Ar ages of eucrites and thermal history of asteroid 4 Vesta. *Meteoritics & Planetary Science* 38:669-710.

Bukovanská M., Ireland T. R., El Goresy A., Palme H., Spettel B., and Wlotzka F. 1991. Zircons in the Padvarnikai brecciated eucrite (abstract). *Meteoritics* 26:325.

Cherniak D. J. and Dimanov A. 2010. Diffusion in pyroxene, mica and amphibole. *Reviews in Mineralogy & Geochemistry* 72:641-690.

Consolmagno G. J. and Drake M. J. 1977. Composition and evolution of the eucrite parent body: Evidence from rare earth elements. *Geochimica et Cosmochimica Acta* 41:1271-1282.

Cotten J., Ledez A., Bau M., Caroff M., Maury R. C., Dulski P., Fourcade S., Bohn M., and Brousse R. 1995. Origin of anomalous Rare-Earth Element and Yttrium enrichments in subaerially exposed basalts - Evidence from French-Polynesia. *Chemical Geology* 119:115-138.

Crozaz G., Floss C. and Wadhwa M. 2003. Chemical alteration and REE mobilization in meteorites from hot and cold deserts. *Geochimica et Cosmochimica Acta* 67:4727-4741.

Dawson P., Hargreave M. M., and Wilkinson G. R. 1971. The vibrational spectrum of zircon ($ZrSiO_4$). *Journal of Physics C: Solid State Physics* 4:240-256.

Dodd R. T. 1981. Meteorites- A Petrologic-Chemical Synthesis. *Cambridge University Press, New York*, New york, USA, 368 p.

Drake M.J. 2001. The eucrite/Vesta story. *Meteoritics & Planetary Science* 36:501-513.

Duke M. B., and Silver L. T. 1967. Petrology of eucrites, howardites and mesosiderites. *Geochimica et Cosmochimica Acta* 31:1637-1665.

Evensen N. M., Hamilton P. J., and O'Nions R. K. 1978. Rare Earth abundances in chondritic meteorites. *Geochimica et Cosmochimica Acta* 42:1199-1212.

Floss C., Crozaz G., Yamaguchi A., and Keil K. 2000. Trace element constraints on the origins of highly metamorphosed Antarctic eucrites. *Antarctic Meteorite Research* 13:222-237.

Freer R. 1981. Diffusion in Silicate Minerals and Glasses: A Data Digest and Guide to the Literature. *Contributions to Mineralogy and Petrology* 76:440-454.

Ganguly J. and Tazzoli V. 1994. Fe^{2+}-Mg interdiffusion in orthopyroxene: Retrival from the data on intracrystalline exchange reaction. *American Mineralogist* 79:930-937.

Geisler T. 2002. Isothermal annealing of partially metamict zircon: evidence for a three-stage recovery process. *Physics and Chemistry of Minerals.* 29:420-429.

Geisler T., Pidgeon R. T., van Bronswijk W., and Pleysier R. 2001. Kinetics of thermal recovery and recrystallization of partially metamict zircon: a Raman spectroscopic study. *European Journal of Mineralogy* 13:1163-1176.

Gounelle M., Chaussidon M., Morbidelli A., Barrat J. A., Engrand C., Zolensky M. E. and McKeegan K. D. 2009. A unique basaltic micrometeorite expands the inventory of solar system planetary crusts. *Proceedings of the National Academy of Sciences of the United States of America* 106:6904-6909.

Greenwood R. C., Franchi I. A., Jambon A., and Buchanan P. C. 2005. Widespread magma oceans on asteroidal bodies in the early Solar System. *Nature* 435:916-918.

Harlow G. E. and Klimentidis R. 1980. Clouding of pyroxene and plagioclase in eucrites: implications for post-crystallization processing. Proceedings, 11th Lunar Science Conference. pp. 1131-1148.

Hoskin P. W. O. and Rodgers K. A. 1996. Raman spectral shift in the isomorphous series $(Zr_{1-x}Hf_x)SiO_4$. *European Journal of Solid State Inorganic Chemistry* 33:1111-1121.

Huebner J. S. and Turnock A. C. 1980. The melting relations at 1bar of pyroxenes composed largely of Ca-, Mg-, and Fe-bearing components. *American Mineralogist* 65:225-271.

Huebner J. S., Ross M., Hickling N. 1973. Partial melting of pyroxenes and the origin of mare basalts (abstract), *Lunar and Planetary Conference* 4:397-399.

Hsu W. and Crozaz G. 1996. Mineral chemistry and the petrogenesis of eucrites: I. Noncumulate eucrites. *Geochimica et Cosmochimica Acta* 60:4571-4591.

Ireland T. R. and Bukovanskà M. 1992. Zircons from the Stannern eucrite (abstract). *Meteoritics* 27:237.

Jochum K. P., Willbold M., Raczeck I., Stoll B., and Herwig K. 2005. Chemical characterisation of the USGS reference glasses GSA-1G, GSC-1G, GSD-1G, GSE-1G, BCR2-G, BHVO2-G, and BIR1-G using EPMA, ID-TIMS, ID-ICP-MS and LA-ICP-MS. *Geostandards and Geoanalytical Research* 29:285-302.

Llorca J., Casanova I., Trigo-Rodriguez J. M., Madeido J. M., Roszjar J., Bischoff A., Ott U., Franchi I. A., Greenwood R. C., and Laubenstein M. 2009. The Puerte Lápice eucrite. *Meteoritics & Planetary Science* 44:159-174.

Mason B., Jarosewich E., and Nelen J. A. 1979. The pyroxene-plagioclase achondrites. *Smithsonian Contributions to the Earth Sciences* 22:27-45.

Mayne R. G., McSween H. Y., Jr., McCoy T. J., Gale A. 2009. Petrology of the unbrecciated eucrites. *Geochimica et Cosmochimica Acta* 73:794-819.

McCord T. B., Adams J. B., and Johnson T.V. 1970. Asteroid Vesta: Spectral reflectivity and compositional implications. *Science* 168:1445-1447.

McSween H. Y. Jr., Mittlefehldt D. W., Beck A. B., Mayne R. G., McCoy T. J. 2010. HED Meteorites and their relationship to the geology of Vesta and Dawn mission. *Space Science Reviews*. 34p.

Metzler, K. 1985. Gefüge und Zusammensetzung von Gesteinsfragmenten in polymikten achondritischen Breccien. *Diploma thesis*, University of Münster, 150 pp.

Metzler K., Bobe K. D., Palme H., Spettel B., and Stöffler D. 1995. Thermal and impact metamorphism on the HED parent asteroid. *Planetary and Space Science* 43:499-525.

Miller M. F. 2002. Isotopic fractionation and the quantification of ^{17}O anomalies in the oxygen three-isotope system: an appraisal and geochemical significance. *Geochimica et Cosmochimica Acta* 66:1881-1889.

Miller M. F., Franchi I. A., Sexton A. S., and Pillinger C. T. 1999. High precision $\delta^{17}O$ isotope measurements of oxygen from silicates and other oxides: Method and Applications. *Rapid Communications in Mass Spectrometry* 13:1211-1217.

Misawa K., Yamaguchi A., and Kaiden H. 2005. U-Pb and ^{207}Pb-^{206}Pb ages of zircons from basaltic eucrites: Implications for early basaltic volcanism on the eucrite parent body. *Geochimica et Cosmochimica Acta* 69:5847-5861.

Mittlefehldt D. W. 2000. Petrology and geochemistry of the Elephant Moraine A79002 diogenite: A genomict breccia containing a magnesian harzburgite component. *Meteoritics & Planetary Science* 35:901-912.

Mittlefehldt D. W. and Lindstrom M. M. 2003. Geochemistry of eucrites: genesis of basaltic eucrites, and Hf and Ta as petrogenetic indicators for altered Antarctic eucrites. *Geochimica et Cosmochimica Acta* 67:1911-1935.

Mittlefehldt D. W., McCoy T. J., Goodrich C. A., and Kracher A. 1998. Non-chondritic meteorites from asteroidal bodies. In *Reviews in Mineralogy*, edited by Papike J. J., vol 36. Washington D. C.: Mineralogical Society of America. pp. 4-1-4-195.

Nasdala L., Irmer G., and Wolf D. 1995. The degree of metamictization in zircon: a Raman spectroscopic study. *European Journal of Mineralogy* 7:471-478.

Nasdala L., Pidgeon R. T., Wolf D. 1996. Heterogeneous metamictization of zircon on a microscale, *Geochimica et Cosmochimica Acta* 60:1091-1997.

Nasdala L., Götze J., Pidgeon R. T., Kempe U., and Seifert T. 1998. Constraining a SHRIMP U-Pb age: microscale characterization of zircons from Saxionian Rotliegende rhyolites. *Contributions to Mineralogy and Petrology* 132:300-306.

Nasdala L., Wenzel M., Varva G., Irmer G., Wenzel T., and Kober B. 2001. Metamictisation of natural zircon: accumulation versus thermal annealing of radioactivity-induced damage. *Contributions to Mineralogy and Petrology* 141:125-144.

Nasdala L., Reiners P.W., Garver J.I., Kennedy A.K., Stern R.A., Balan E., and Wirth R. (2004) Incomplete retention of radiation damage in zircon from Sri Lanka. *American Mineralogist* 89: 219-231.

Palenik C. S., Nasdala L., and Ewing R. C. 2003. Radiation damage in zircon. *American Mineralogist* 88:777-781.

Powell M. A., Walker D., and Hays J. F. 1980. Experimental solidification of a eucrite basalt: Microprobe studies (abstract). *Lunar and Planetary Science* 11:896-898.

Pun A. and Papike J. J. 1996. Unequilibrated eucrites and the equilibrated Juvinas eucrite: Pyroxene REE systematics and major, minor, and trace element zoning. *American Mineralogist* 81:1438-1451.

Righter K. and Drake M. J. 1997. A magma ocean on Vesta: core formation and petrogenesis of eucrites and 471 diogenites. *Meteoritics & Planetary Science* 32:929-944.

Roeder P. L. and Reynolds I. 1991. Crystallization of chromite and chromium solubility in basaltic melts. *Journal of Petrology* 32:909-934.

Roszjar J., Metzler K., Bischoff a., Greenwood R. C., and Franchi I. A. 2009a. Northwest Africa (NWA) 5073 - An eucritic basalt with cm-sized pyroxenes (abstract). *Meteoritics & Planetary Science* 44:5202.

Roszjar J., Geisler T., Scherer E. E., and Bischoff A. 2009b. The thermal history of zircon from the NWA5073 eucrite as revealed by Raman spectroscopy (abstract). *Meteoritics & Planetary Science* 44:5203.

Roszjar J., Srinivasan G., Bischoff A., Mezger K., and Whitehouse M. 2009c. Hf-W ages of zircons - New constraints on the evolution of the eucrite parent body (abstract #1655), 40th *Lunar and* Planetary Science Conference.

Roszjar J. and Scherer E. E. 2010. Lu-Hf systematics of the NWA 5073 eucrite reflect a complex thermal history (abstract). *Meteoritics & Planetary Science* 45:5425.

Rubin A. E. 1992. A shock-metamorphic model for silicate darkening and compositionally variable plaglioclase in CK and ordinary chondrites. *Geochimica et Cosmochimica Acta* 56:1705-1714.

Ruzicka A., Snyder G. A. and Taylor L. A. 1997. Vesta as the howardite, eucrite and diogenite parent body: 477 implications for the size of a core and for large-scale differentiation. *Meteoritics & Planetary Science* 32:825-840.

Saiki K., Takeda H., and Tagei T. 1990. Zircon in magnesian, basaltic eucrite Yamato 791438 and its Possible Origin (abstract). *Lunar and Planetary Science* 21:341-349.

Scott E. R. D., Greenwood R. C., Franchi I. A. and Sanders I. S. 2009. Oxygen isotopic constraints on the origin 489 and parent bodies of eucrites, diogenites, and howardites. *Geochimica et Cosmochimica Acta* 73: 5835-5853.

Stelzner T., Heide K., Bischoff A., Weber A., Weber D., Scherer P., Schukz L., Happel M., Schrön W., Neupert U., Michel R., Clayton R. N., Mayeda T. K., Bonani G., Haidas I., Ivy-Ochs S., and Suter M. 1999. In interdisciplinary study of weathering effects in ordinary chondrites from the Acfer region Algeria, *Meteoritics & Planetary Science* 34:787-794.

Stolper E. 1977. Experimental petrology of eucritic meteorites. *Geochimica et Cosmochimica Acta* 41:587-611.

Stöffler D., Bischoff A., Buchwald V., and Rubin A. E. 1988. Shock effects in meteorites. In *Meteorites and the Early Solar System,* edited by Kerridge J. F. and Matthews J. F., Tucson: University of Arizona Press, pp. 165-202.

Stöffler D., Keil K., and Scott E. R. D. 1991. Shock metamorphism of ordinary chondrites. *Geochimica et Cosmochimica Acta* 55:3845-3867.

Takeda H. 1979. A layered-crust model of a howardite parent body. *Icarus* 40:455-470.

Takeda H. 1991. Comparison of Antarctic and non-Antarctic achondrites and possible origin of the differences. *Geochimica et Cosmochimica Acta* 55:35-47.

Takeda H., and Yanai K. 1982. Mineralogical examination of the Yamato 79 achondrites: polymict eucrites and ureilites. Proceedings 7th Symposium on Antarctic meteorites. pp. 97-123.

925 Takeda H. and Graham A. L. 1991. Degree of equilibrium of eucritic pyroxenes and thermal
926 metamorphism of the earliest planetary crust. *Meteoritics* 26:129-134.
927
928 Takeda H., Mori H., Yanai K., and Wooden J. L. 1982. Three different basalt types in Antarctic
929 polymict eucrites, a view from pyroxene chemical zoning trend (abstract), *Lunar and Planetary*
930 *Science* 13:792-293.
931
932 Takeda H., Mori H., Delaney J. S., Prinz M., Harlow G. E., and Ishii T. 1983. Mineralogical
933 comparison of antarctic and non-antarctic HED (howardites-eucrites-diogenites) achondrites.
934 Proceedings, 8th Symposium on Antarctic Meteorites. pp. 181-205.
935
936 Takeda H., Mori H., and Bogard D. D. 1994. Mineralogy and ^{39}Ar-^{40}Ar age of an old pristine basalt:
937 Thermal history of the HED parent body. *Earth and Planetary Science Letters* 122:183-194
938
939 Tanabe K. and Hiraishi J. 1980. Correction of finite slit width effects on Raman line widths.
940 *Spectrochimica Acta Part A: Molecular Spectroscopy* 36:341-344.
941
942 Walker D., Powell M. A., Lofgren G. E., and Hays J. F. 1978. Dynamic crystallization of a eucritic
943 basalt. Proceedings, 9th *Lunar and Planeary. Science Conference.* pp. 1369-1391.
944
945 Warren P. H. 1997. Magnesium oxide-iron oxide mass balance constraints and a more detailed model
946 for the 502 relationship between eucrites and diogenites *Meteoritics & Planetary Science* 32:945–
947 963.
948
949 Warren P. H. 2002. Northwest Africa 1000: A new eucrite with maskelynite, unequilibrated pyroxene
950 crisscrossed by fayalite-rich veins, and Stannern-like geochemistry (abstract #1147). 33rd *Lunar*
951 *and Planetary Science Conference.*
952
953 Warren P. H. and Jerde E. 1987. Composition and origin of Nuevo Laredo trend eucrites. *Geochimica*
954 *et Cosmochimica Acta* 51:713-725.
955
956 Warren P. H. and Kallemeyn G. W. 2001. Eucrite Bluewing 001: a Stannern-like bulk composition
957 and its linkage with other unequilibrated HED basalts (abstract). *Lunar and Planetary Science*
958 32:2114.
959
960 Warren P. H., Jerde E. A., Migdisova L. F., Yaroshevsky A. A. 1990. Pomozdino: An anomalous,
961 high-MgO/FeO, yet REE-rich eucrite, Proceedings, 20th Lunar and Planetary Science Conference.
962 pp. 281-297.
963
964 Warren P. H., Kallemeyn G. W., Huber H., Ulff-Møller F., and Choe W. 2009. Siderophile and other
965 geochemical constraints on mixing relationships among HED-meteorite breccias. *Geochimica et*
966 *Cosmochimica Acta* 73:5918-5943.
967
968 Wiechert U. H., Halliday A. N., Palme H., and Rumble D. 2004. Oxygen isotope evidence for rapid
969 mixing of the HED parent body. *Earth and Planetary Science Letters* 221:373-382.
970
971 Wlotzka F. 1993. A weathering scale for the ordinary chondrites (abstract). *Meteoritics* 28:460.
972
973 Wopenka B., Jolliff B. L., Zinner E., and Kremser R. 1996. Trace element zoning and incipient
974 metamictization in a lunar zircon: Application of three microprobe techniques. *American*
975 *Mineralogist* 81:902-912.
976
977 Yamaguchi A. and Mikouchi T. 2005. Heating experiments of the HaH 262 eucrite and implication for
978 the metamorphic history of highly metamorphosed eucrites (abstract). *Lunar and Planetary Science*
979 36: 1574 (CD).
980

Yamaguchi A. and Misawa K. 2001. Occurrence and possible origin of zircon in basaltic eucrites (abstract). *Antarctic Meteorites* 26:165-166.

Yamaguchi A., Taylor G. J., and Keil K. 1996. Global metamorphism on the eucrite parent body. *Icarus* 124:97-112.

Yamaguchi A., Taylor G. J., Keil K., Floss C., Crozaz G., Nyquist L. E., Bogard D. D., Garrison D. H., Wiesmann H., and Shih C.-Y. 2001. Post-crystallization reheating and partial melting of eucrite EET90020 by impact into the hot crust of asteroid 4 Vesta ~4.50 Ga ago. *Geochimica et Cosmochimica Acta* 65:3577-3599.

Yamaguchi A., Clayton R. N., Mayeda T. K., Ebihara M., Oura Y., Miura Y. N., Haramura H., Misawa K., Kojima H. and Nagao K. 2002. A new source of basaltic meteorites inferred from Northwest Africa 011. *Science* 296:334-336.

Yamaguchi A., Barrat J. A., Greenwood R. C., Shirai N., Okamoto C., Setoyanagi T., Ebihira M., Franchi I. A., and Bohn M. 2009. Crustal partial melting on Vesta: Evidence from highly metamorphosed eucrites. *Geochimica et Cosmochimica Acta* 73:7162-7182.

Zhang M., Salje E. K. H., Farnan I., Graeme-Barber A., Daniel P., Ewing R. C., Clark A. M., Rios S., and Leroux H. 2000a. Metamictization of zircon: Raman spectroscopic study. *Journal of Physics: Condensed Matter* 12:97-112.

Zhang M., Salje E. K. H., Farnan I., Capitani G. C., Leroux H., Clark A. M., Schlüter J., and Ewing R. C. 2000b. Annealing of a-decay damage in zircon: a Raman spectroscopic study. *Journal of Physics: Condensed Matter* 12:3131-3148.

Zhang M., Salje E. K. H., Ewing R. C., Farnan I., Rios S., Schlüter J., and Leggo P. 2000c. Alpha-decay damage and recrystallization in zircon: evidence for an intermediate state from infrared spectroscopy. *Journal of Physics: Condensed Matter* 12:5189-5199.

Table 1. Modal abundance of major phases and mesostasis in NWA 5073 (vol.%).

Pyroxene phenocrysts	24.8
Primary feldspars (plagioclases)	26.4
Small pyroxenes	39.9
Mesostasis	8.5
Metal	0.4

Table 2. Chemical composition of mineral phases in NWA 5073. Results in wt.%.

	SiO_2	TiO_2	Al_2O_3	Cr_2O_3	FeO*	MnO	MgO	CaO	Na_2O	K_2O	P_2O_5	HfO_2	ZrO_2	Y_2O_3	Total	Endmembers average	Endmembers min. – max.
Major phases																	
Pyroxene cores (n=27)	52.4	0.11	1.11	1.01	18.0	0.62	24.3	1.85	0.02	<0.01	n.d.	n.d.	n.d.	n.d.	99.41	$En_{55.1}Wo_{4.2}Fs_{40.7}$	$En_{51.0\text{-}60.0}Wo_{1.7\text{-}7.6}Fs_{34.0\text{-}45.0}$
Pyroxene rims (n=27)	49.6	0.34	1.11	0.57	25.9	1.04	12.9	8.2	0.03	<0.01	n.d.	n.d.	n.d.	n.d.	99.68	$En_{27.5}Wo_{17.4}Fs_{55.1}$	$En_{19.8\text{-}34.1}Wo_{8.2\text{-}33.8}Fs_{42.2\text{-}62.4}$
Small pyroxenes (n=11)	49.5	0.24	1.07	0.63	29.4	1.17	12.5	5.5	0.02	<0.01	n.d.	n.d.	n.d.	n.d.	100.01	$En_{26.4}Wo_{11.6}Fs_{62.0}$	$En_{22.8\text{-}35.8}Wo_{5.9\text{-}18.8}Fs_{58.3\text{-}68.8}$
Pyroxenes mesostasis (n=5)	49.8	0.42	0.73	0.23	19.2	0.68	9.3	19.7	0.04	0.02	n.d.	n.d.	n.d.	n.d.	100.15	$En_{27.1}Wo_{41.4}Fs_{31.5}$	$En_{25.7\text{-}27.9}Wo_{33.7\text{-}44.8}Fs_{27.7\text{-}40.7}$
Large Plagioclases (n=47)	47.4	0.02	32.3	<0.01	0.39	<0.01	0.10	16.9	1.65	0.16	n.d.	n.d.	n.d.	n.d.	99.00	$An_{84.2}Ab_{14.9}Or_{0.9}$	$An_{77.0\text{-}88.9}Ab_{11.0\text{-}20.1}Or_{0.1\text{-}2.9}$
Plagioclases mesostasis (n=5)	51.0	0.03	30.1	0.02	0.65	<0.01	0.04	14.6	2.49	0.44	n.d.	n.d.	n.d.	n.d.	99.42	$An_{74.4}Ab_{23.0}Or_{2.6}$	$An_{77.7\text{-}76.8}Ab_{20.4\text{-}24.9}Or_{2.0\text{-}3.5}$
Secondary Plagioclase (n=17)	43.0	n.d.	35.7	n.d.	1.38	n.d.	0.12	19.7	0.12	<0.01	n.d.	n.d.	n.d.	n.d.	100.00	$An_{98.6}Ab_{1.3}Or_{0.1}$	$An_{97.2\text{-}100}Ab_{0\text{-}2.8}Or_{0\text{-}0.3}$
Minor phases																	
Chromite (n=5)[§]	<0.1	3.2	12.6	47.9	33.9	0.76	0.84	<0.1	n.d.	n.d.	n.d.	n.d.	n.d.	n.d.	99.78		
Ilmenite (n=13)[§]	<0.1	53.7	n.d.	<0.1	44.1	1.17	0.53	n.d.	n.d.	n.d.	n.d.	n.d.	n.d.	n.d.	99.81		
Apatite (n=19)	<0.01	n.d.	n.d.	n.d.	0.72	n.d.	<0.01	54.1	<0.01	n.d.	41.8	n.d.	n.d.	0.11	99.23		
Zircon (n=10)	32.4	n.d.	n.d.	n.d.	1.58	0.02	n.d.	0.06	n.d.	n.d.	0.14	1.31	66.2	0.16	101.83		
Tridymite (n=7)	98.9	0.07	0.23	0.03	0.36	<0.01	<0.01	0.13	<0.01	0.02	n.d.	n.d.	n.d.	n.d.	99.20		
Fe-rich olivine veins (n=16)	31.9	<0.01	0.06	0.19	53.1	1.46	14.4	0.05	<0.01	<0.01	n.d.	n.d.	n.d.	n.d.	101.13	$Fo_{32.5}Fa_{67.5}$	$Fo_{29\text{-}35}Fa_{65\text{-}71}$
	Fe	**Ni**	**Co**	**Cu**	**Cr**	**Zn**	**Ca**	**Si**	**Mg**	**Mn**	**Na**	**K**	**S**				
Metal cores (n=13)	99.08	<0.01	0.16	<0.02	<0.02	<0.01	0.05	0.03	<0.01	<0.01	<0.01	<0.02	<0.02		99.33		

Data were obtained by EPMA; n.d. = not detected; *all Fe as FeO; zircon: Al was always below detection limit, high Fe content probably caused by contamination from surrounding phases such as ilmenite and Fe-metal; apatites: Cl and F average values are 0.3 and 4.0 wt.%, respectively; [§] Data obtained by SEM; chromite: V_2O_3 = 0.61 wt.%, ilmenite: V_2O_3 = 0.3 wt.%; for ilmenite and chromite: Ni was always below detection limit.

Table 3. Major and trace element composition of NWA 5073, compared to Stannern, Bouvante, and Nuevo Laredo. Oxides in wt.%, trace elements in μg/g. Eu/Eu* and La_n/Yb_n* are calculated relative to CI average given by Evensen et al. (1978).

	NWA 5073	**Stannern**	**Bouvante**	**Nuevo Laredo**
Mass (g)	0.098	1.0	1.47	1.0 g
TiO_2	0.77	1.08	1.06	0.94
Al_2O_3	10.38	12.26	11.60	12.36
Cr_2O_3	0.587	0.33	0.33	0.30
FeO	20.13	18.58	20.07	20.91
MnO	0.58	0.55	0.50	0.63
MgO	8.70	6.98	6.26	5.70
CaO	9.46	10.99	10.40	10.90
Na_2O	0.52	0.56	0.56	0.48
K_2O	0.09	0.09	0.10	0.06
P_2O_5	0.097	0.10	0.14	0.09
Li	11.06	12.39	13.51	11.68
Be	0.32	0.44	0.42	0.37
Sc	25.8	30.2	30.8	35.8
V	78.51	56.90	55.20	60.10
Co	8.04	3.83	7.00	2.87
Ni	1.32	1.1	0.33	3.70
Cu	2.43	5.07	0.88	0.25
Zn	0.98	2.80	1.42	1.17
Ga	1.14	1.51	1.6	1.69
Rb	0.34	0.58	0.61	0.37
Sr	2131	92.7	93.7	84.4
Y	22.17	32.13	33.00	26.22
Zr	70.1	101	99.6	70.0
Nb	6.85	8.20	7.74	5.38
Cs	0.008	0.016	0.023	0.017
Ba	176	52.65	56.17	39.03
La	4.18	5.58	5.65	3.85
Ce	10.59	14.4	14.37	10.10
Pr	1.57	2.15	2.18	1.52
Nd	7.79	10.76	10.79	7.64
Sm	2.42	3.48	3.46	2.57
Eu	0.617	0.840	0.786	0.768
Gd	3.18	4.44	4.47	3.44
Tb	0.561	0.787	0.793	0.614
Dy	3.62	5.24	5.37	4.13
Ho	0.78	1.15	1.15	0.920
Er	2.22	3.26	3.26	2.67
Yb	2.04	3.06	2.87	2.56
Lu	0.291	0.434	0.421	0.366
Hf	1.77	2.51	2.52	1.83
Ta	0.365	0.441	0.413	0.292
W	0.193	0.174	0.165	0.105
Pb	0.24	(1.59)	0.32	0.26
Th	0.548	0.700	0.699	0.488
U	0.162	0.177	0.182	0.116
Eu/Eu*	0.68	0.65	0.61	0.79
La_n/Yb_n*	1.38	1.23	1.33	1.02

Table 4. LA-ICP-MS data of silicates in NWA 5073. Results in µg/g.

Pyroxene cores	1	2	3	4	5	6	7	8	single Px*	average (n=8)
La	0.010	0.025	0.005	0.005	0.013	0.007	0.021	0.008	0.366	0.012
Ce	0.032	0.058	0.027	0.016	0.047	0.024	0.050	0.028	1.302	0.035
Pr	0.009	0.013	0.004	0.004	0.010	0.004	0.010	0.008	0.276	0.008
Nd	0.066	0.081	0.027	0.029	0.068	0.032	0.063	0.064	1.726	0.054
Sm	0.068	0.054	0.020	0.037	0.059	0.020	0.048	0.050	0.883	0.044
Eu	0.011	0.008	0.004	0.007	0.008	0.005	0.009	0.008	0.054	0.007
Gd	0.127	0.143	0.038	0.062	0.098	0.055	0.095	0.117	1.486	0.092
Dy	0.244	0.240	0.067	0.131	0.169	0.096	0.171	0.228	2.297	0.168
Er	0.235	0.219	0.060	0.118	0.148	0.099	0.154	0.208	1.597	0.155
Yb	0.295	0.290	0.072	0.151	0.184	0.149	0.221	0.270	1.865	0.204
Lu	0.055	0.051	0.013	0.025	0.031	0.023	0.038	0.045	0.281	0.035

Plagioclase	1	2	3	4	5	6	7	average (n=7)
La	0.243	0.350	0.522	0.308	0.328	0.286	0.194	0.319
Ce	0.523	0.834	1.029	0.602	0.692	0.702	0.397	0.683
Pr	0.064	0.101	0.124	0.076	0.087	0.088	0.053	0.085
Nd	0.295	0.463	0.584	0.323	0.388	0.400	0.254	0.387
Sm	0.099	0.133	0.164	0.095	0.089	0.126	0.081	0.112
Eu	2.006	2.100	2.528	1.950	1.980	2.074	1.930	2.081
Gd	0.067	0.124	0.154	0.082	0.083	0.101	0.064	0.096
Dy	0.052	0.120	0.157	0.078	0.069	0.123	0.047	0.092
Er	0.022	0.054	0.071	0.046	0.040	0.062	0.028	0.046

* single small, Fe-rich -pyroxene, found in close association to a mesostasis area; not used for average pyroxene calculation.

Table 5. U and Th concentrations, calculated α-decay dose, and frequencies and linewidths (FWHM) of the $\nu_3(SiO_4)$. Raman band of analyzed zircon grains from the NWA 5073 eucrite.

Zircon no.	U (ppm)	± 2σ	Th (ppm)	± 2σ	Dose (10^{16} α-events/mg)*	± 2σ *1	Frequency (cm^{-1})*2	FWHM (cm^{-1})*2
Z1	<23	-	<20	-	<0.067		1000.5	9.9
Z3	<30	-	<20	-	<0.086		1001.2	8.5
Z4	<29	-	24	21	<0.093		1003.2	7.6
Z5	71	29	42	21	0.243	0.091	996.8	17.2
Z6	123	29	71	21	0.421	0.092	996.6	21.6
Z8	78	30	<21	-	0.255	0.096	999.3	12.1
Z9	105	29	86	21	0.372	0.092	998.2	18.8
Z10	75	30	<21	-	0.246	0.096	997.9	17.9
Z11	104	29	<21	-	0.334	0.092	997.2	25.8
Z13	160	29	120	21	0.559	0.092	991.7	25.3

*The dose was calculated for an inferred age of 4555 Ma; *1Errors do not include the error of the inferred age;

Figure Captions:

Fig. 1: (a) Sawn surface of a section from the 185 g main mass of NWA 5073. **(b)** Thin section of NWA 5073; transmitted light, crossed polarizers.

Fig. 2: Ternary phase diagram for pyroxenes (Px) analyzed in NWA 5073. Large pyroxenes preserved their initial magmatic signature, as seen by Mg-enriched pigeonite cores. The chemical composition of small pyroxenes is in the range of the rims of large pyroxene phenocrysts or even more Fe-enriched. Pyroxenes found in the mesostasis are clearly distinct as they are significantly enriched in Ca. For comparison, composition of pristine and metasomatized pyroxenes from NWA 2061 (dark gray, solid-lined areas) and Y-75011 (light gray, dashed-lined areas) are shown, as these two eucrites also contain secondary Ca-rich plagioclase. The latter data are taken from Barrat et al. (2011).

Fig. 3: BSE images of the bulk texture of NWA 5073 (a) and textural details of its Fe-rich olivine veins (b-d). **(a)** Mosaic of BSE images from a NWA 5073. (b-d) Detailed images illustrating prominent Fe-rich olivine veins that crosscut large pyroxene laths, while adjacent silikate grains are devoid of them. **(b)** Typical zoned pyroxene lath with $En_{57}Wo_5$ in the crystals core and $En_{28}Wo_{17}$ at the rim is crosscut by Fe-rich olivine veins that end abruptly towards adjacent plagioclases (Plg) and smaller pyroxenes (Px). **(c)** Pyroxene-plagioclase border that shows a clear restriction of Fe-rich olivine veins to large pyroxene crystals. **(d)** Enlarged Mg-rich core region of a large pyroxene lath that is crosscut by Fe-rich olivine veins (Fa_{67}) and Fe-diffusion pathways along cleavage planes. Olivine veins are often occupied by small chromite, and troilite (FeS) grains, and Sr-sulfate inclusions, with the latter being a weathering product. Fe-rich areas that are aligned parallel to the olivine veinlets are probably formed by solid-state Fe-diffusion.

Fig. 4: BSE images of secondary phases in NWA 5073. **(a)** and **(b)**: Fe-rich olivine veins (Ol) in large pyroxene (Px) and Fe-diffusion paths into their pyroxene host along cleavage planes: Cc = calcite (terrestrial weathering). **(c)** and **(d)**: Secondary, Ca-rich plagioclase typically 5-20 µm in diameter that were usually found in close association with Fe-rich olivine veins (Ol), are highlighted in ellipses. They are chemically distinct to adjacent large plagioclase (Plg).

Fig. 5: Ternary feldspar diagram illustrating three distinct plagioclase (Plg) types. Small plagioclase grains, located in the mesostasis, are slightly more Ab-rich (An_{72-77}) compared to larger plagioclase laths, which scatter to slightly higher An values (An_{72-89}). Secondary plagioclase is extremely enriched in Ca with An_{97-100}.

Fig. 6: BSE images **(a)** and **(c)** of representative zircon grains (Zr), selected for µ-Raman spectroscopy and EPMA analyses. Zircon grains typically occur in association with ilmenite (Ilm), plagioclase (Plg), Ca-pyroxene (Ca-Px), and silica (SiO_2). Corresponding cathodoluminescence images are given in **(b)** and **(d)**. Zircon positions are highlighted as dashed areas.

Fig. 7: Diagram for bulk rock TiO_2 vs. FeO_{total}/MgO of basaltic, including residual, eucrite samples. The field of the basaltic eucrites has been drawn from a compilation of more than 170 analyses mainly from Warren et al. (2009), references listed in Barrat et al. (2007), and the residual eucrites from Yamaguchi et al. (2009). Residual eucrites cannot be distinguished from the basaltic eucrites in this diagram.

Fig. 8: Rare Earth Element (REE) abundances relative to CI chondritic abundance (Evensen et al., 1978), given for NWA 5073 bulk rock in comparison to Stannern, NWA4523, Juvinas, and Nuevo Laredo.

Fig. 9: Trace element pattern for NWA 5073 bulk rock compared to the Stannern-trend eucrites, including Stannern and NWA 4523, and Nuevo Laredo and Juvinas eucrites. All data are given relative to the Juvinas eucrite. Sr and Ba values of NWA 5073 whole rock are high (2131 and 176 ppm, respectively), probably due to terrestrial weathering (Stelzner et al., 1999) and thus are excluded from this diagram.

Fig. 10: REE pattern for plagioclase and pyroxene grains analyzed in NWA 5073. Average plagioclase (n=7) is shown by black squares, minimum and maximum values of all analyzed plagioclase grains are reported within the data range highlighted in light gray. The average of pigeonite cores (n=8) is given by white triangles. Data range for all analyzed pigeonite cores is highlighted in dark gray. One single small, Fe-rich pyroxene (light gray circles), closely associated with a mesostasis area, is extremely enriched in REE (Lu 10×CI). This analysis has not been used for average pyroxene core calculation.

Fig. 11: Oxygen isotope data for NWA 5073 compared to other eucrites (monomict, polymict, and cumulate eucrites), howardites, diogenites, and angrites. $\Delta^{17}O$ values are linearized (Miller, 2002). In this $\Delta^{17}O$ versus $\delta^{18}O$ diagram, samples formed from a homogeneous reservoir that subsequently fractionated by mass-dependent processes, plot along horizontal lines. Silicate minerals on Earth have isotopic compositions consistent with mass-dependent fractionation from a single reservoir, and define the terrestrial fractionation line (TFL). Angrites define a second horizontal line, the angrite fractionation line (AFL), with a mean $\Delta^{17}O$ value of -0.072 ± 0.007 (1σ). If polymict breccias are excluded, remaining HED samples also show limited $\Delta^{17}O$ variation and define a single eucrite fractionation line (EFL) with a mean $\Delta^{17}O$ value of -0.239 ± 0.007 (1σ). Diagram modified after Greenwood et al. (2005).

Fig. 12: Representative Raman spectra of five single zircon grains in sample NWA 5073 reveal a decreased frequency and an increased broadening of the $\nu_3(SiO_4)$ stretching band near ~1008 cm^{-1} (dashed line) with increasing radiation dose (*D*). The calculated α–dose, given within 2σ uncertainties, and expressed per 10^{16} × α-decay events/mg sample, is shown close to the spectra for each zircon crystal Single zircon analyses are presented relative to a pure, synthetic, crystalline zircon (gray), taken from the RRUFF Raman data base.

Fig. 13: (a) Diagram of the frequency of the $\nu_3(SiO_4)$ band analyzed in ten zircon crystals in NWA 5073 plotted against the measured linewidth of this band (given as full width at half maximum, FWHM). The radiation damage trend (RDT, gray field) is defined by variably, self-irradiation-damaged, terrestrial zircons (Saxonian rhyolites and Sri Lanka zircons data from Nasdala et al., 1998; 2004; Zhang et al., 2001a, b; own unpubl. data). A synthetic, non-metamict zircon is also plotted . Recent episodic annealing of heavily metamict zircon would shift the data points to the upper right in this diagram (highlighted by arrows), as indicated by dry heating experiments (Geisler et al., 2001; Geisler, 2002). **(b)** Plot of the linewidth (FWHM) of the $\nu_3(SiO_4)$ band vs. the α-decay dose (calculated accumulated radiation dose) for all analyzed zircon grains in NWA 5073. Uncertainties are in the range of 2σ. All data points plot below the radiation damage accumulation curve defined by Palenik et al. (2003), unambiguously indicating post-crystallization thermal annealing. Note that annealing of the NWA 5073 zircons is also obvious when compared with the Saxonian rhyolite zircons, which have neither episodically nor continuously been annealed (Nasdala et al., 1998) and were used to determine the damage accumulation curve. For more details of how the damage accumulation curve was defined see Palenik et al. (2003).

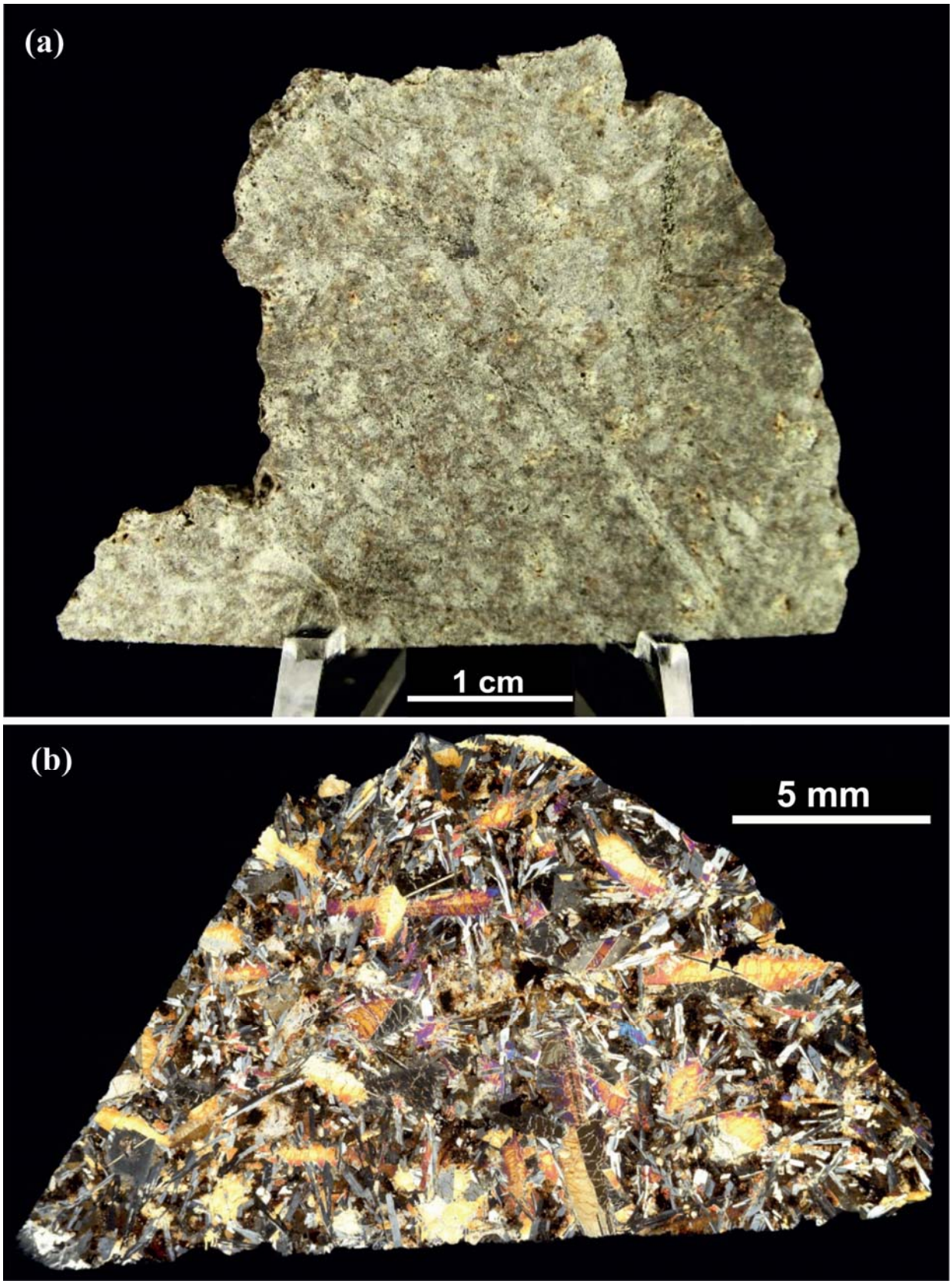

Fig.1

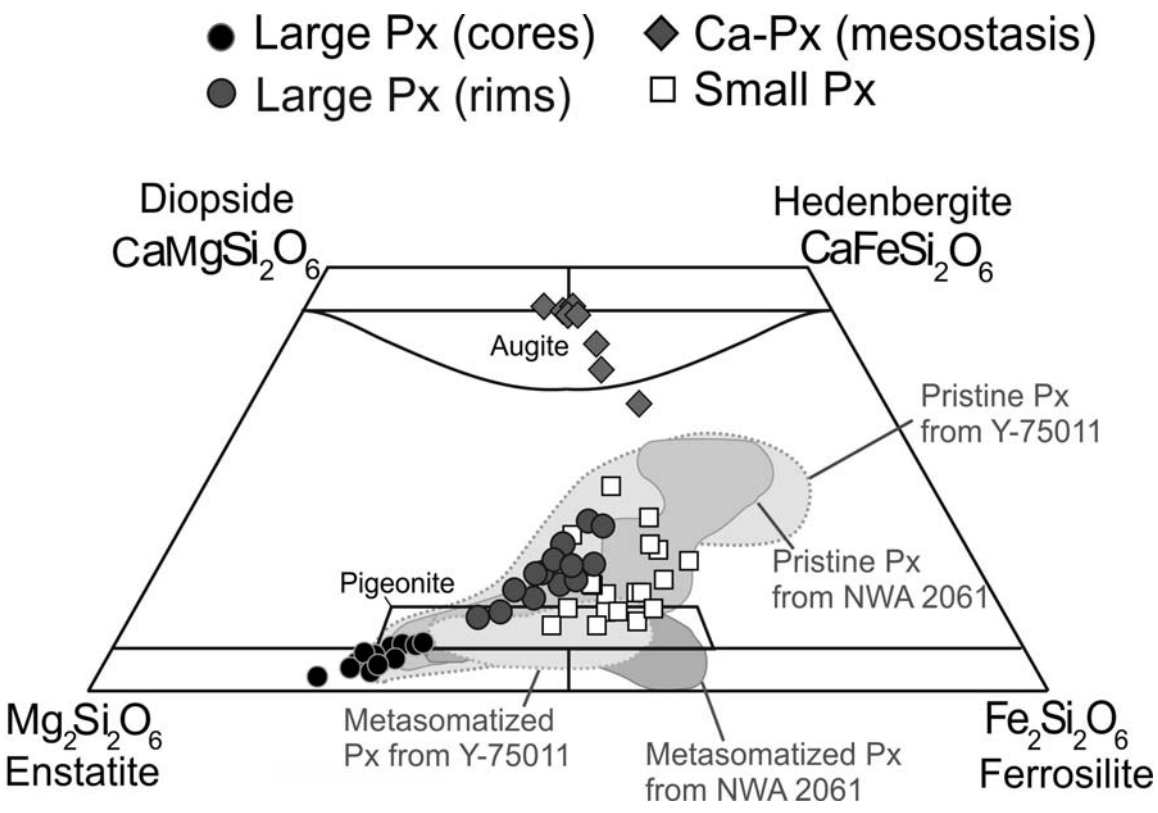
Large Px (cores)
Large Px (rims)
Ca-Px (mesostasis)
Small Px
Diopside
CaMgSi2O6
Hedenbergite
CaFeSi2O6
Augite
Pristine Px
from Y-75011
Pristine Px
from NWA 2061
Pigeonite
Metasomatized
Px from Y-75011
Metasomatized Px
from NWA 2061
Mg2Si2O6
Enstatite
Fe2Si2O6
Ferrosilite

Fig.2

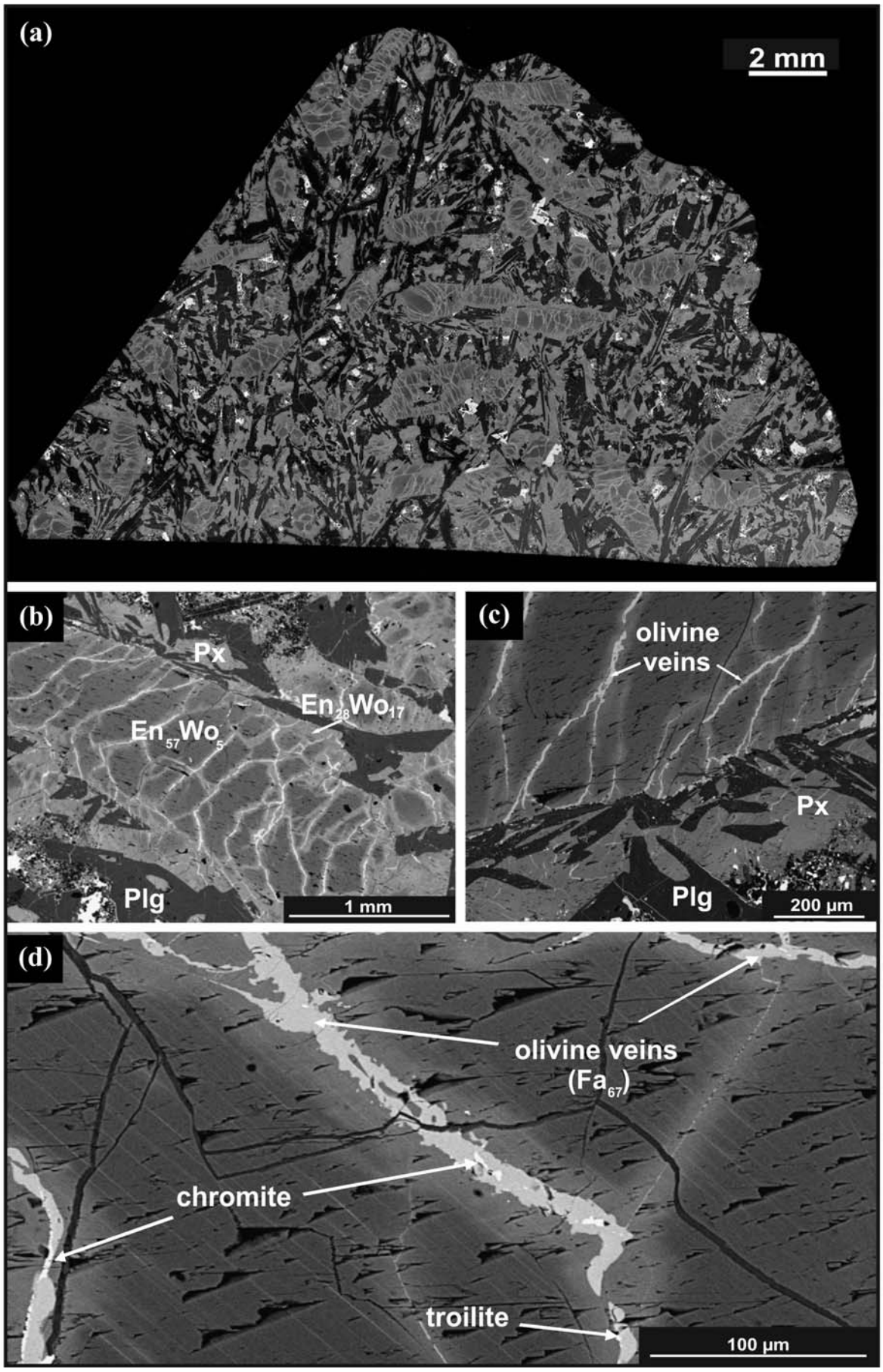
(a)
2 mm
(b)
Px
$En_{28}Wo_{17}$
$En_{57}Wo_{5}$
Plg
1 mm
(c)
olivine
veins
Px
Plg
200 µm
(d)
olivine veins
(Fa_{67})
chromite
troilite
100 µm

Fig.3

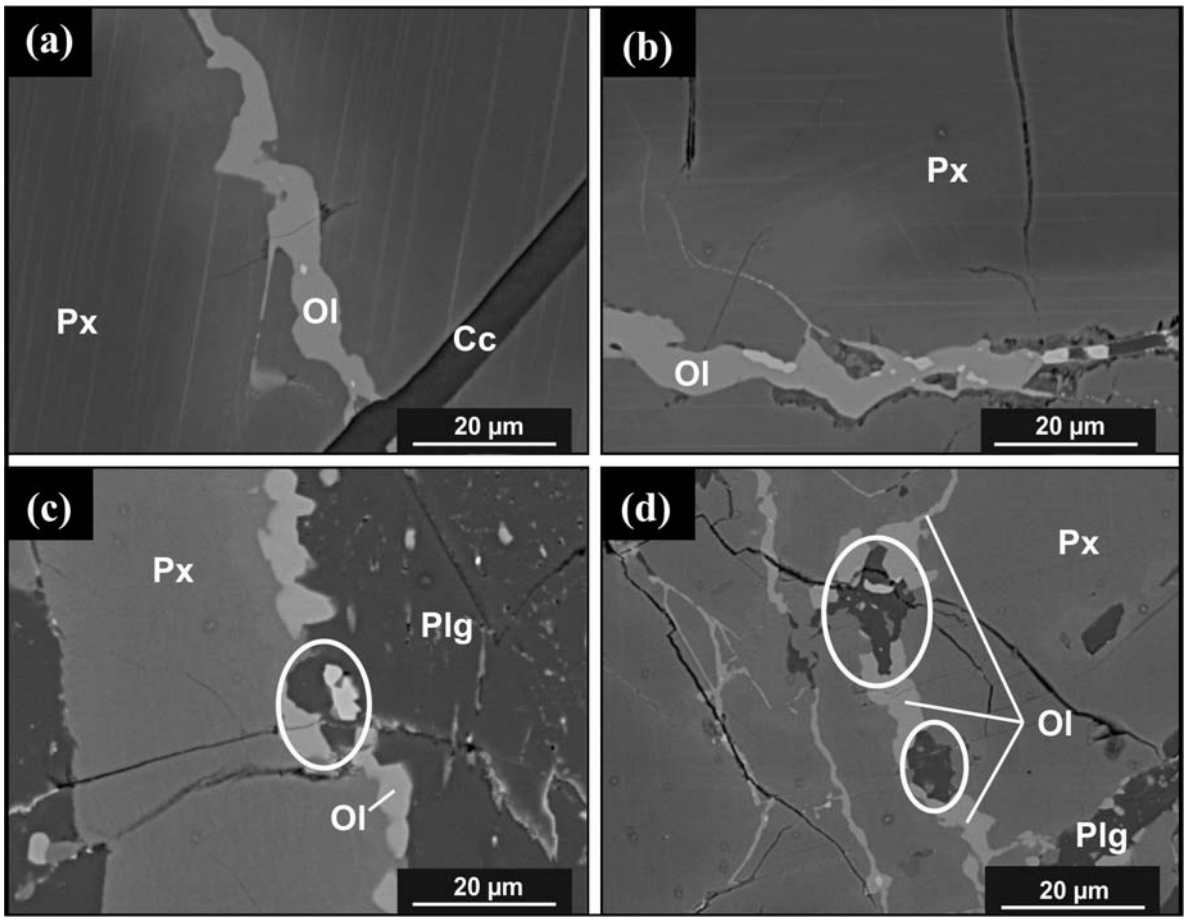
(a)
Px
Ol
Cc
20 µm
(b)
Px
Ol
20 µm
(c)
Px
Plg
Ol
20 µm
(d)
Px
Ol
Plg
20 µm

Fig.4

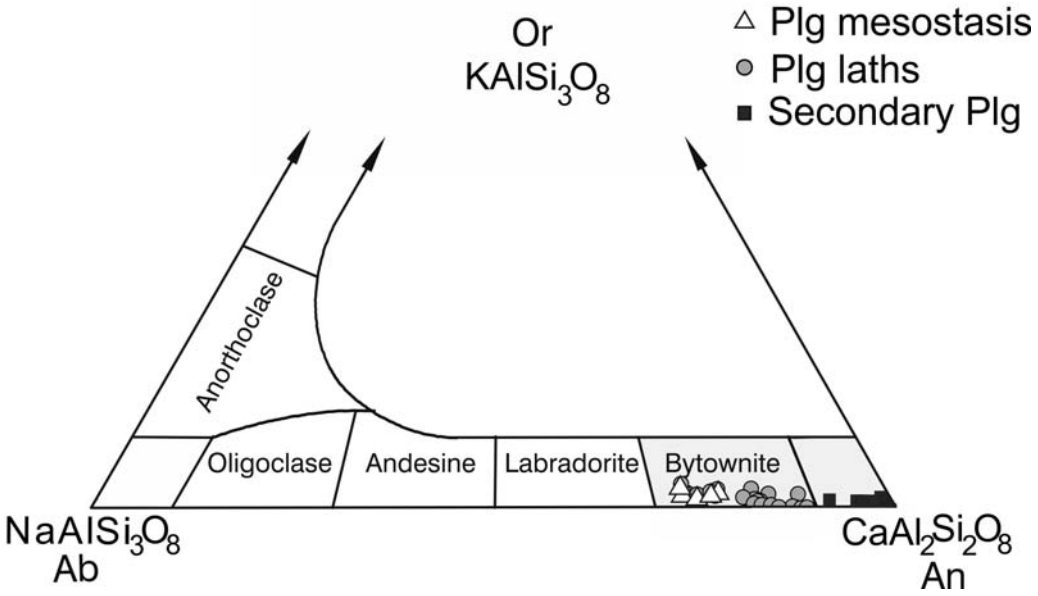
Or
KAlSi3O8
Plg mesostasis
Plg laths
Secondary Plg
Anorthoclase
Oligoclase
Andesine
Labradorite
Bytownite
NaAlSi3O8
Ab
CaAl2Si2O8
An

Fig.5

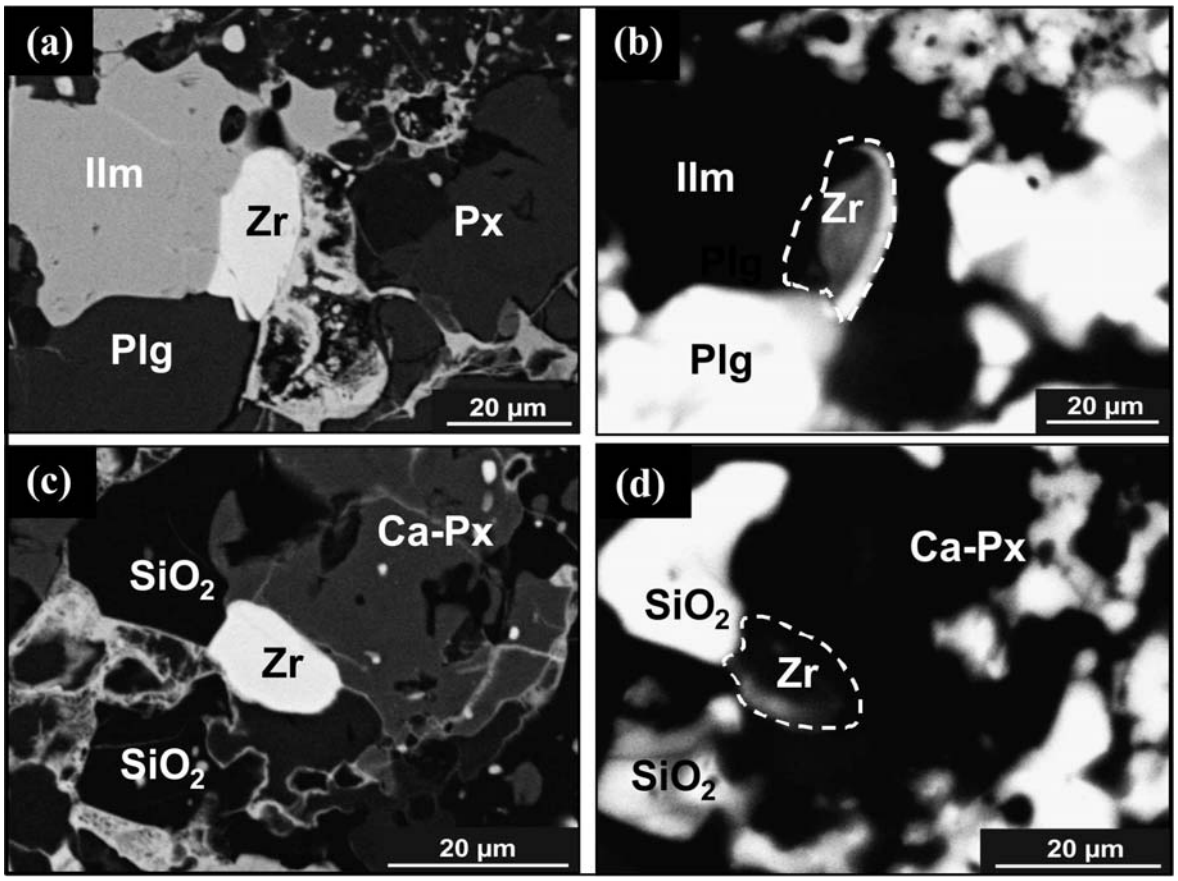
(a)
Ilm
Zr
Px
Plg
20 μm
(b)
Ilm
Zr
Plg
Plg
20 μm
(c)
Ca-Px
SiO2
Zr
SiO2
20 μm
(d)
Ca-Px
SiO2
Zr
SiO2
20 μm

Fig.6

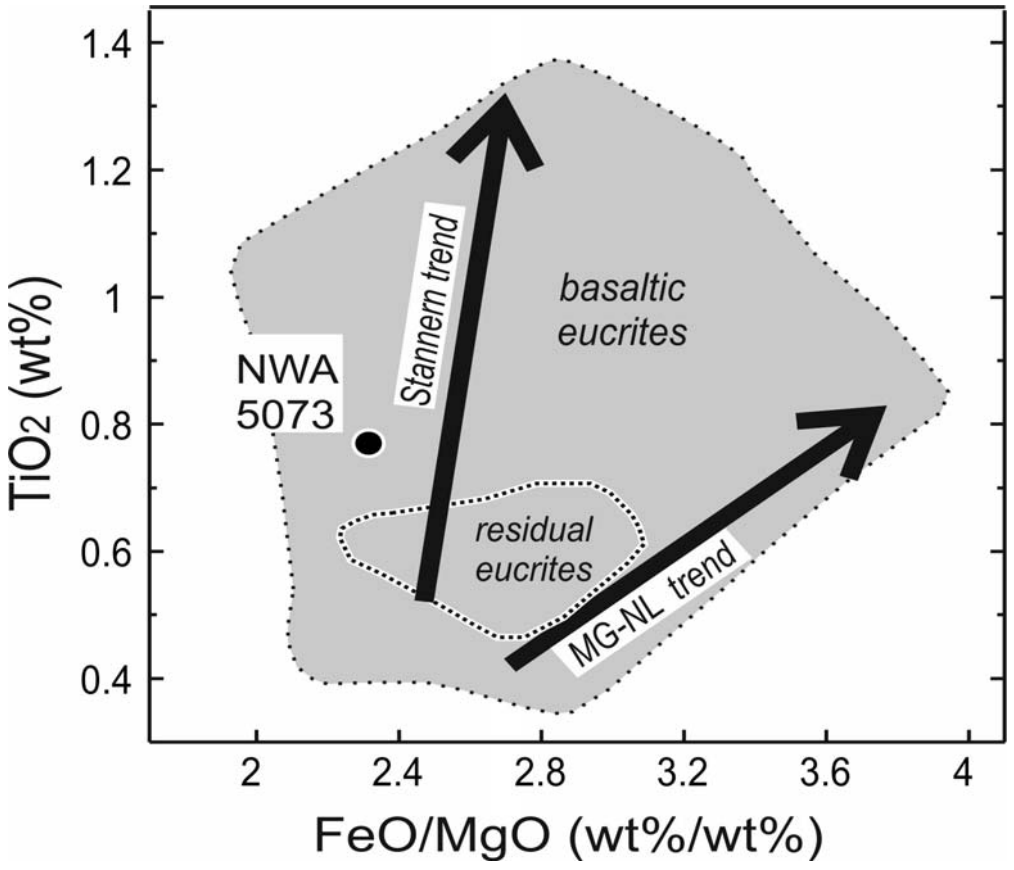
1.4
1.2
1
0.8
0.6
0.4
TiO2 (wt%)
2
2.4
2.8
3.2
3.6
4
FeO/MgO (wt%/wt%)
basaltic
eucrites
Stannern trend
NWA
5073
residual
eucrites
MG-NL trend

Fig.7

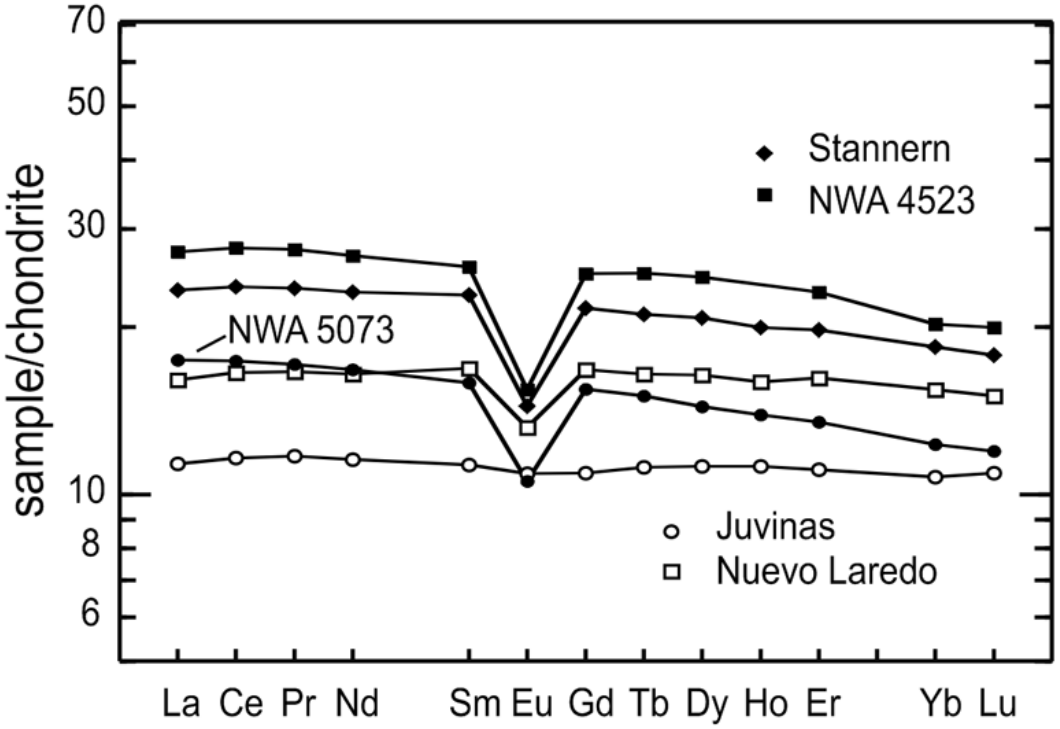
70
50
30
10
8
6
sample/chondrite
Stannern
NWA 4523
NWA 5073
Juvinas
Nuevo Laredo
La Ce Pr Nd Sm Eu Gd Tb Dy Ho Er Yb Lu

Fig.8

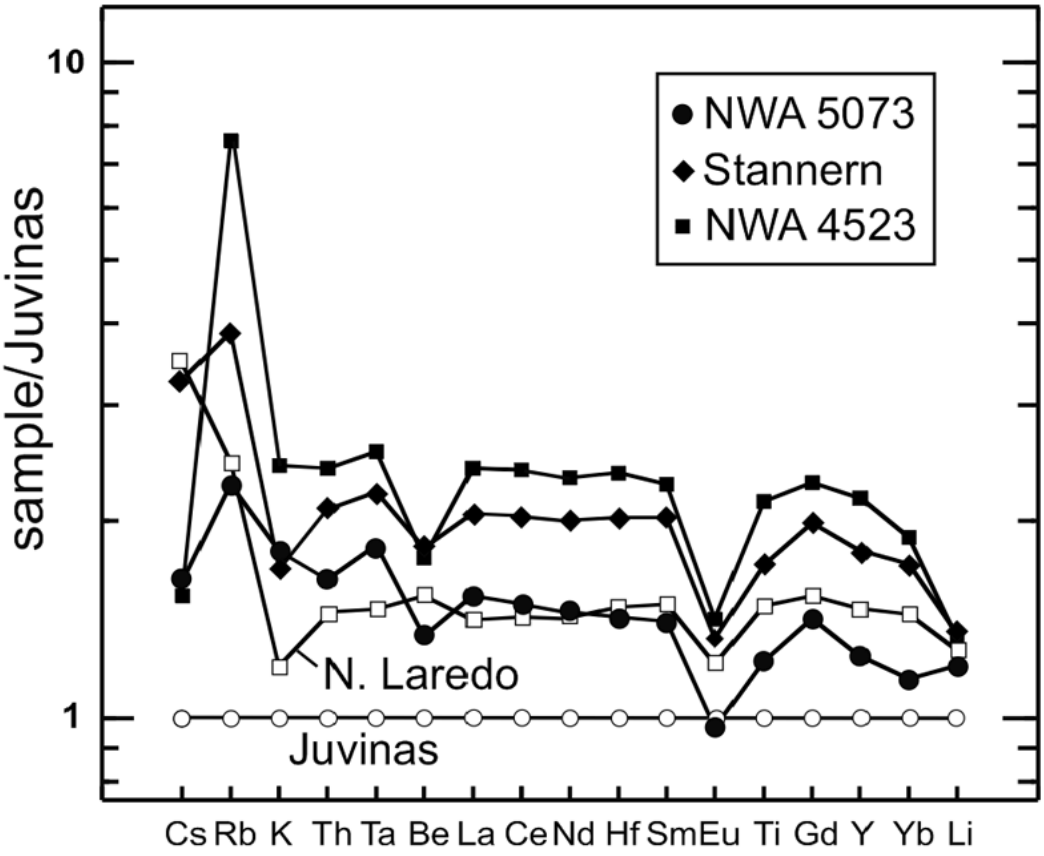
10
1
sample/Juvinas
NWA 5073
Stannern
NWA 4523
N. Laredo
Juvinas
Cs Rb K Th Ta Be La Ce Nd Hf Sm Eu Ti Gd Y Yb Li

Fig.9

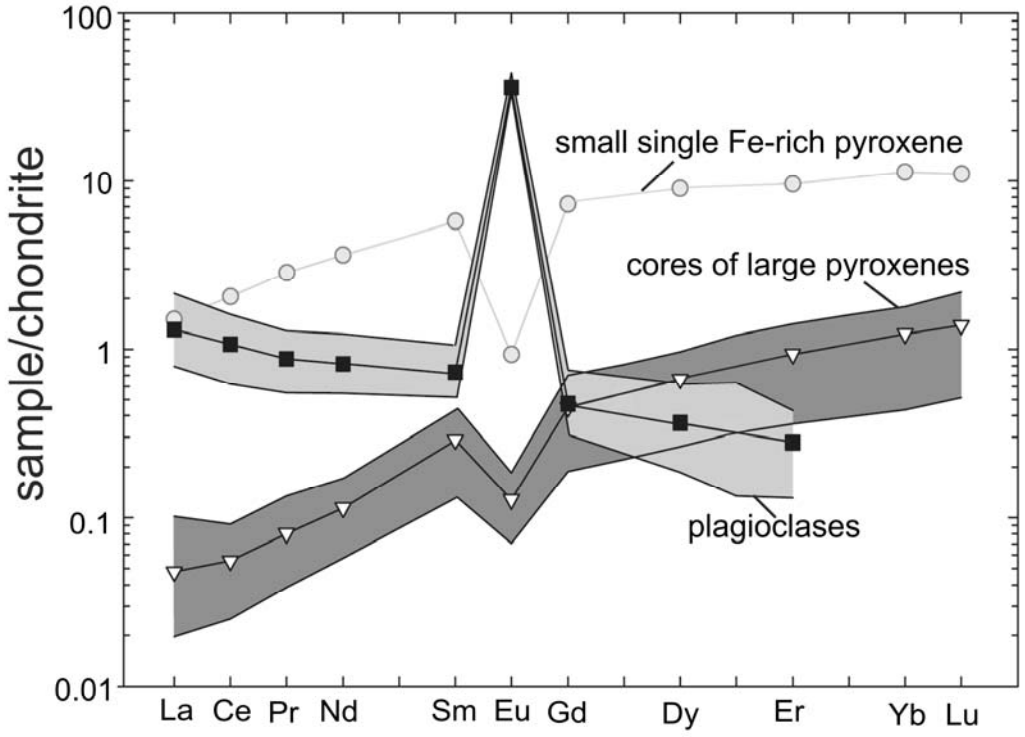
100
10
1
0.1
0.01
sample/chondrite
small single Fe-rich pyroxene
cores of large pyroxenes
plagioclases
La Ce Pr Nd Sm Eu Gd Dy Er Yb Lu

Fig.10

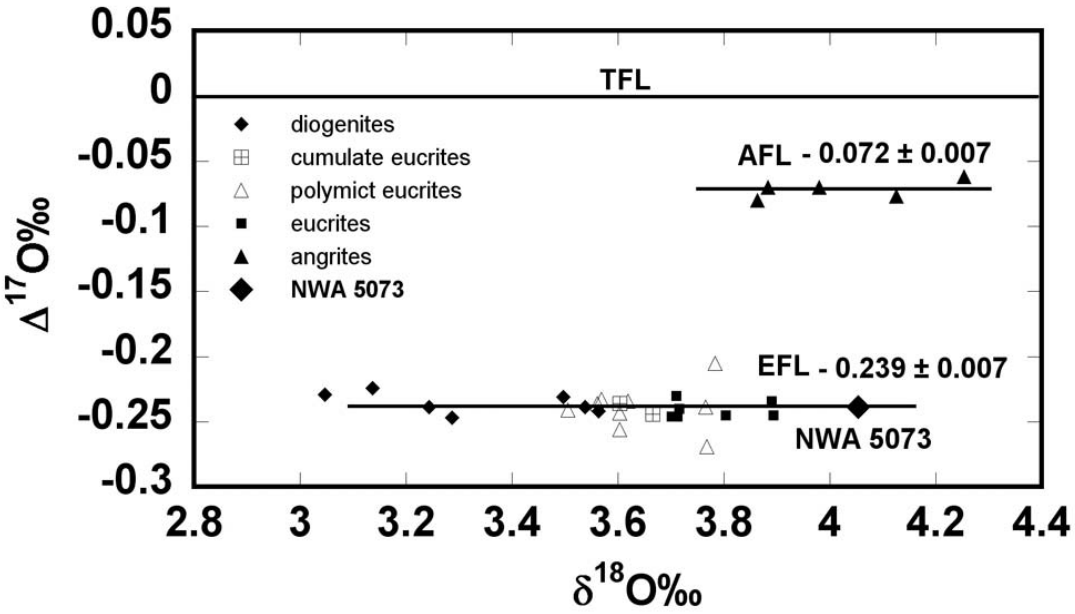
0.05
0
-0.05
-0.1
-0.15
-0.2
-0.25
-0.3
TFL
diogenites
cumulate eucrites
polymict eucrites
eucrites
angrites
NWA 5073
AFL - 0.072 ± 0.007
EFL - 0.239 ± 0.007
NWA 5073
2.8 3 3.2 3.4 3.6 3.8 4 4.2 4.4
Δ17O‰
δ18O‰

Fi.11

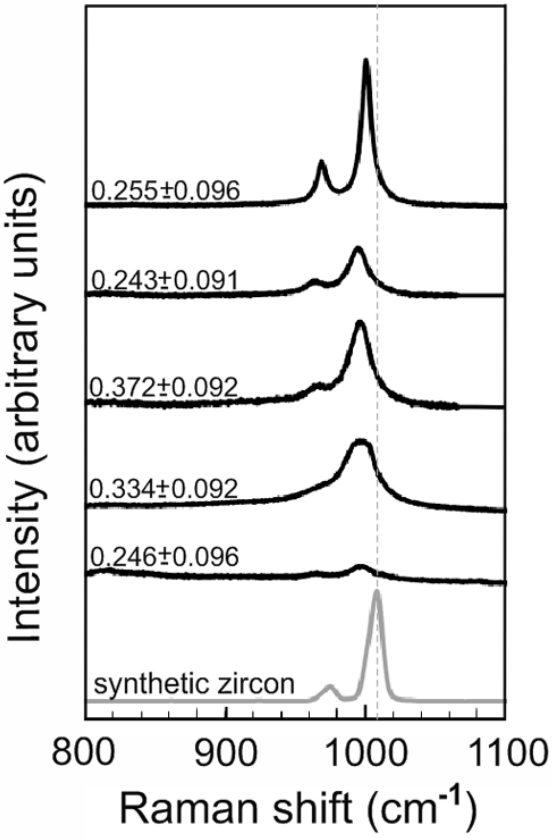
0.255±0.096
0.243±0.091
0.372±0.092
0.334±0.092
0.246±0.096
synthetic zircon
Intensity (arbitrary units)
800
900
1000
1100
Raman shift (cm-1)

Fig.12

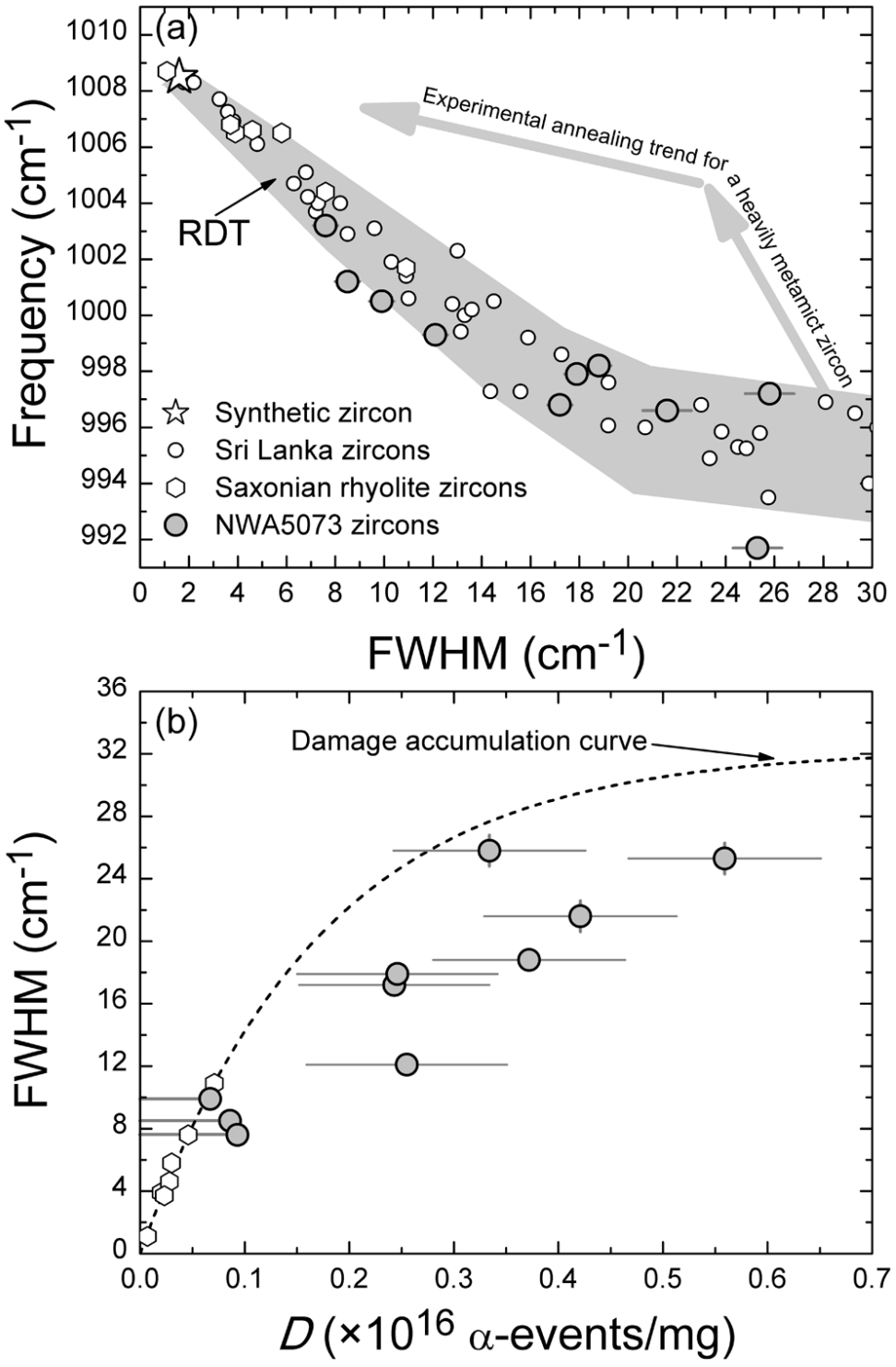
(a)
Frequency (cm-1)
FWHM (cm-1)
RDT
Experimental annealing trend for a heavily metamict zircon
Synthetic zircon
Sri Lanka zircons
Saxonian rhyolite zircons
NWA5073 zircons
(b)
Damage accumulation curve
FWHM (cm-1)
D (×10^16 α-events/mg)

Fig.13